Implications of garnet nucleation overstepping for the P-T evolution of the Lesser Himalayan Sequence of central Nepal

Published version:

DOI:10.1111/jmg.12695

Groppo Chiara (Orcid ID: 0000-0002-4174-6613)
Tamang Shashi (Orcid ID: 0000-0001-6529-6197)

IMPLICATIONS OF GARNET NUCLEATION OVERSTEPPING FOR THE P-T EVOLUTION OF THE LESSER HIMALAYAN SEQUENCE OF CENTRAL NEPAL

Shashi Tamang[1,2], Chiara Groppo[1,3]*, Frédéric Girault[2], Franco Rolfo[1,3]

[1]Department of Earth Sciences, University of Torino, via Valperga Caluso 35, 10125 Torino, Italy
[2]Université Paris Cité, Institut de Physique du Globe de Paris, CNRS, 1 rue Jussieu, F-75005 Paris, France
[3]CNR-IGG, via Valperga Caluso 35, 10125 Torino, Italy

Running title: Garnet nucleation overstepping and P-T evolution in the Lesser Himalayan Sequence of central Nepal

Corresponding Author
Chiara Groppo
Department of Earth Sciences, University of Torino, via Valperga Caluso 35, 10125 Torino, Italy
CNR-IGG, via Valperga Caluso 35, 10125 Torino, Italy
chiara.groppo@unito.it

Authors details
Shashi Tamang
Department of Earth Sciences, University of Torino, via Valperga Caluso 35, 10125 Torino, Italy
shashi.tamang@unito.it

Frédéric Girault
Université Paris CIté, Institut de Physique du Globe de Paris, CNRS, 1 rue Jussieu, F-75005 Paris, France
girault@ipgp.fr

Franco Rolfo

This article has been accepted for publication and undergone full peer review but has not been through the copyediting, typesetting, pagination and proofreading process which may lead to differences between this version and the Version of Record. Please cite this article as doi: 10.1002/jmg.12695

Department of Earth Sciences, University of Torino, via Valperga Caluso 35, 10125 Torino, Italy
CNR-IGG, via Valperga Caluso 35, 10125 Torino, Italy
franco.rolfo@unito.it

IMPLICATIONS OF GARNET NUCLEATION OVERSTEPPING FOR THE P-T EVOLUTION OF THE LESSER HIMALAYAN SEQUENCE OF CENTRAL NEPAL

Shashi Tamang[1,2], Chiara Groppo[1,3]*, Frédéric Girault[2], Franco Rolfo[1,3]

[1]Department of Earth Sciences, University of Torino, via Valperga Caluso 35, 10125 Torino, Italy
[2]Université Paris Cité, Institut de Physique du Globe de Paris, CNRS, 1 rue Jussieu, F-75005 Paris, France
[3]CNR-IGG, via Valperga Caluso 35, 10125 Torino, Italy

Running title: Garnet nucleation overstepping and P-T evolution in the Lesser Himalayan Sequence of central Nepal

Abstract

Recent studies have demonstrated that kinetic factors can significantly influence garnet nucleation, delaying its appearance with respect to the equilibrium predictions. Overstepping of garnet nucleation occurs in both contact and regional metamorphic settings, with extremely variable degrees: the factors controlling such highly variable degrees of overstepping are still unclear. This study focuses on garnet nucleation and growth in aluminous metapelites from the Barrovian inverted metamorphic pile of the upper portion of the Lesser Himalayan Sequence (Upper-LHS; central Nepal), with the aim of: (i) investigating if (and how) the bulk rock composition can influence overstepping of garnet nucleation, and (ii) which are the implications of garnet nucleation overstepping for the P-T evolution of a Barrovian metamorphic sequence.

Detailed petrographic, microstructural and compositional data are presented for six phyllitic schists, containing porphyroblasts of garnet, staurolite and/or kyanite. Their P-T evolution is constrained through thermodynamic forward modelling (i.e. isochemical phase diagrams combined with isopleth thermobarometry), assuming that equilibrium was attained at every stage of their metamorphic evolution. Comparison between the P-T conditions inferred for the growth of garnet core, the assemblages predicted to be stable at these P-T conditions, and the modelled garnet-in reaction boundary, suggests that the studied samples have experienced different degrees of apparent thermal (ΔT) and/or baric (ΔP) overstepping of garnet nucleation. We suggest that the bulk-rock MnO and CaO amounts might have influenced the apparent ΔT and ΔP overstepping of the garnet-in reaction: more specifically, the higher the bulk-rock MnO content, the more pronounced the apparent ΔT overstepping, whereas the lower the bulk-rock CaO content, the greater the ΔP overstepping. However, rather than an effective delay of garnet appearance with respect to equilibrium predictions, the apparent ΔT overstepping of garnet nucleation could reflect the attainment of the critical 0.5% threshold of garnet abundance, below which garnet is not readily detected in thin section. Kinetic factors seem much less critical in controlling the growth of the garnet rim at peak P-T conditions, confirming that peak metamorphic conditions constrained through equilibrium approaches based on the composition of garnet rim and of the matrix assemblage can be considered as reliable. Overall, the P-T paths of the studied samples are characterized by prograde heating coupled with tectonic overload (peak-P conditions of 9.5–10.5 kbar, 580–590°C), followed by heating during exhumation (peak-T conditions of 8.2–8.9 kbar, 610–630 °C), supporting those thermo-mechanical models that predict a period of slowdown (or quiescence) of the Main Central Thrust activity.

Keywords: forward thermodynamic modelling, overstepping of garnet nucleation, Barrovian metamorphism, P-T evolution, Upper Lesser Himalayan Sequence, aluminous metapelites

1. INTRODUCTION

Barrovian-type metamorphic sequences are widespread in both ancient and modern collisional orogenic belts, being the result of crustal thickening induced by continent collision. The forward thermodynamic modelling approach, based on the principles of equilibrium thermodynamics, is currently routinely applied to constrain their P-T evolution, which is crucial for our understanding of the mountain building processes. Aluminous metapelites from Barrovian garnet- and staurolite- zones are particularly suitable for this aim, because they generally develop specific assemblages as a function of P-T conditions; moreover, application of isopleth thermobarometry to garnet-bearing aluminous metapelites is a powerful method for tightly constraining their P-T evolution, due to the relatively common preservation of prograde growth zoning within garnet porphyroblasts (e.g. Tinkham & Ghent, 2005). The reliability of thermobarometric methods based on equilibrium thermodynamics has been recently questioned by a number of studies which demonstrate that garnet nucleation can be significantly influenced by kinetic factors, resulting in a delay of garnet appearance with respect to the equilibrium predictions. Initially discussed as a relevant process in contact metamorphic settings (e.g. Waters & Lovegrove, 2002; Pattison & Tinkham, 2009), the overstepping of garnet nucleation is being more and more frequently reported also in regional metamorphic terranes, including Barrovian metamorphic settings (e.g. Pattison et al., 2011; Spear et al., 2014; Carlson et al., 2015; Spear & Wolfe, 2019). Studies specifically focused on understanding the relative importance of equilibrium vs. kinetic –controlled garnet nucleation in Barrovian metamorphic terranes, show that the apparent degree of overstepping of garnet nucleation can be extremely variable, ranging from minimal (<10 °C and 0.5 kbar; e.g. Gaidies et al., 2008, 2015; Moynihan & Pattison, 2013; George & Gaidies, 2017; Gaidies & George, 2021), to moderate (<30°C and 1 kbar; e.g. Spear et al., 2014) or pronounced (>30°C and 2 kbar; e.g. Spear et al., 2014; Spear & Wolfe, 2019). The factors controlling such highly variable degrees of overstepping of garnet nucleation are still unclear (Nagurney et al., 2021).

This study focuses on garnet nucleation and growth in aluminous metapelites from the upper portion of the Lesser Himalayan Sequence (Upper-LHS) of the Ganesh Himal region in central Nepal. The Lesser Himalayan Sequence (LHS) experienced Barrovian metamorphism during the Himalayan orogenic cycle, developing an inverted metamorphic gradient ranging from the chlorite to the biotite, garnet, staurolite and kyanite zones (e.g. Pêcher, 1989; Kohn, 2014; Goscombe et al., 2018; Waters et al., 2019). We focus our attention on the uppermost structural levels of the LHS (Upper-LHS), where studies have shown that peak metamorphic temperatures up to 630–650°C have been reached, consistent with the sporadic occurrence of staurolite and/or kyanite -bearing lithologies (e.g. Macfarlane, 1995; Rai et al., 1998; Catlos et al., 2001; Khanal et al., 2020; Kohn et al., 2001; Goscombe et al., 2006, 2018; Kohn, 2008; Groppo et al., 2009; Martin et al., 2010; Imayama et al., 2010; Corrie & Kohn, 2011; Mosca et al., 2012; Rolfo et al., 2015; Rapa et al., 2016, 2018). Our aims are threefold: (i) to test the reliability of thermobarometric methods based on equilibrium thermodynamics applied on aluminous metapelites from the same metamorphic domain; (ii) to understand to what extent garnet nucleation in aluminous metapelites can be influenced by kinetic factors, and explore whether the difference in bulk rock composition might control the different degrees of apparent overstepping; and (iii) to constrain the P-T metamorphic evolution of the Upper-LHS in this key area and discuss the results in the framework of the existing thermo-mechanical models used to explain the inverted metamorphism in the LHS.

The P-T paths for the samples were constrained using an isochemical phase diagram modelling approach combined with isopleth thermobarometry. This approach reproduces the observed blastesis-deformation relationships and yields late prograde and peak P-T conditions that are consistent among the six samples, suggesting that kinetic factors did not significantly influence the growth of the garnet rims at peak P-T conditions. Conversely, the estimated early prograde P-T conditions are not consistent for all the samples suggesting that, in some of them, garnet nucleation could have occurred after significant overstepping. We find a strong correlation between the bulk-rock MnO content and the apparent ΔT overstepping of the garnet-in reaction. However, we also find that the apparent ΔT overstepping of garnet nucleation could reflect the attainment of the critical 0.5% threshold of garnet abundance, rather than representing a failure of garnet to nucleate at equilibrium conditions. The apparent ΔP overstepping of garnet nucleation could be instead related to the bulk-rock CaO content. Overall, the P-T paths reconstructed for the studied Upper-LHS samples are characterized by prograde heating coupled with tectonic overloading, followed by moderate heating during exhumation. These “clockwise” paths support those thermo-mechanical models that predict a period of slowdown (or quiescence) of the Main Central Thrust activity.

2. GEOLOGICAL SETTING

In the Nepal Himalaya, the Lesser Himalayan Sequence (LHS) forms a belt up to 100 km wide and quite continuous in western and central Nepal, while it is much thinner and less continuous in eastern Nepal (Fig. 1a). The LHS is a thick Paleo- to Meso-Proterozoic sedimentary sequence originally deposited on the northern margin of the Indian plate (e.g. Gansser, 1964; Parrish & Hodges, 1996; DeCelles et al., 2000; Martin et al., 2005), locally intruded by Proterozoic igneous lithologies (e.g. Kohn et al., 2010; Larson et al., 2017, 2019). During the Himalayan orogeny, this Proterozoic sedimentary sequence was variably deformed and metamorphosed developing a typical inverted metamorphism, with metamorphic grade increasing from south to north and from lower to upper structural levels (e.g. Pêcher, 1989; Kohn, 2014).

In the Himalayan fold-thrust belt, the LHS is tectonically interposed between the underlying Siwalik Group to the south and the overlying Greater Himalayan Sequence (GHS) to the north, from which it is separated by the Main Boundary Thrust (MBT) and the Main Central Thrust (MCT), respectively (Yin & Harrison, 2000) (Fig. 1a). The structure of the LHS is dominated by a regional-scale structural culmination (i.e. the Lesser Himalayan Duplex; De Celles et al., 2001; Pearson & DeCelles, 2005), identified by the occurrence of a broad antiform developed longitudinally with respect to the belt. The interplay between thrusting, folding and erosion led to the present wider exposure of the LHS in western and central Nepal compared to that of eastern Nepal (e.g. Dhital, 2015), where the LHS crops out in large antiformal tectonic windows (Fig. 1a).

The precise location of the main tectonic discontinuity juxtaposing the GHS over the LHS (i.e. the MCT) is still debated, because a plethora of different criteria (structural, metamorphic, chronological, compositional; see for instance Searle et al., 2008 for a review) have been used to define it. In this paper, we follow the definition proposed by Goscombe et al. (2006, 2018), namely: (i) the boundary between the LHS and GHS is mostly a lithostratigraphic boundary (i.e. Himalayan Unconformity HU; see also Kohn, 2014), separating two sequences with different and unique provenance; (ii) rather than being a discrete thrust, the MCT is a broad high strain shear zone (i.e. Main Central Thrust Zone: MCTZ) which affects both the upper structural levels of the LHS and the lower structural levels of the GHS; and (iii) the lower boundary of the MCTZ is marked by two distinct tectonic discontinuities, recognized all along the Himalayan belt: the Main Central Thrust (or Basal Main Central Thrust according to Goscombe et al., 2018) at upper structural levels, mostly coincident with the HU (Fig. 1b,d), and the Ramgarh Thrust (as defined in central and western Nepal by DeCelles et al., 2000 and Robinson et al., 2001), or Munsiari Thrust (in Garhwal, NW India; Valdiya, 1980) at lower structural levels (Fig. 1b,d).

The studied samples were collected in the Upper-LHS unit exposed in the Ganesh Himal region of central Nepal (Fig. 1b; GPS coordinates in Table 1). According to the classification proposed by Stöcklin (1980) and Upreti (1999), in this region the following formations are exposed from the bottom to the top of the Upper-LHS sequence (Fig. 1c,d): Nourpul Formation, Dhading Dolomite and Benighat Slates. The Nourpul Formation is a lithologically heterogeneous succession mostly consisting of phyllites, graphitic schists, quartzites, and carbonatic lithologies (calcic phyllites, calcschists and dolomitic marbles), alternated in metric to decametric layers (Fig. 1c), and appearing at the outcrop scale as thickly banded and variegated in colour (Fig. 2a). The transition from the Nourpul Formation to the overlying Dhading Dolomite is gradual and marked by a progressive increase of the carbonatic lithologies. The Dhading Dolomite mostly consists of fine-grained dolomitic marbles with intercalations of calcschists, carbonatic phyllites and minor graphitic schists (Fig. 1c). The uppermost Benighat Slates is dominated by dark phyllites and calcic metapelites (Fig. 2c), with abundant intercalations of graphitic slates (Fig. 2d), and minor carbonatic lithologies (calcschists and impure marbles) and quartzites (Fig. 1c).

3. METHODS

3.1 Petrography, mineral chemistry and bulk compositions

The studied samples have been collected along two different transects, in the upper part of the Ankhu (samples 17a-) and Trisuli (samples 15a-) valleys, respectively (Fig. 1b). Samples 17a-22 and 15a-15b (Fig. 2a,b) belong to the Nourpul Formation, whereas samples 17a-34, 17a-33, 15a-28b and 17a-42 (Fig. 2c-f) belong to the uppermost Benighat Slates. At the outcrop scale, all the studied samples show a pervasive foliation, locally crenulated (Fig. 2b), and are characterized by the presence of one or more porphyroblastic phase(s) (garnet, staurolite and/or kyanite) (Fig. 2b,e,f).

Petrographic investigations and compositional analysis are summarized in Figs. 3–7. High-resolution multispectral maps were collected on the entire thin sections (ca. 3 × 1.5 cm) in order to obtain the modal compositions of each sample and to highlight their microstructures at the thin section scale (Fig. 3). These X-ray maps were obtained using a JEOL IT300LV Scanning Electron Microscope (SEM) at the Department of Earth Sciences, University of Torino, Italy. The instrument is equipped with an energy dispersive spectrometry (EDS) Energy 200 system and an SDD X-Act3 detector (Oxford Inca Energy, UK). Operating conditions used for mapping are: 15 kV accelerating voltage, process time 1, 2.5 µm point step and 500 ms pixel dwell time. The raw data were processed using the MultiSpec© software (Purdue Research Foundation, USA) in order to obtain the modal compositions.

The rock-forming minerals were analysed with the same SEM-EDS instrument. Operating conditions are: 15 kV accelerating voltage, process time 2 and 30 s counting time. SEM-EDS quantitative data were acquired and processed using the Microanalysis Suite Issue 12, INCA Suite version 4.01; natural mineral standards were used to calibrate the raw data; the ΦρZ correction (Pouchou & Pichoir, 1988) was applied. Mineral chemistry results, only briefly summarized here, are presented in the Supplementary Material; Fig. 6 and Supplementary Tables SM1a-f report the whole set of compositional data for all the minerals analysed in each sample. All the analyses were recalculated using the NORM computer software (Ulmer, 1986); structural formulae have been calculated on the basis of 12 oxygens for garnet, 11 oxygens for muscovite and biotite, 48 oxygens for staurolite, 8 oxygens for plagioclase and 28 oxygens for chlorite. Compositional profiles (Fig. 3 and Supplementary Fig. SM1) were carried out on two (samples 17a-22 and 15a-15b) or three (samples 17a-33 and 17a-42) garnet porphyroblasts, except for sample 15a-28b for which a single, cm-sized, garnet was analysed. In all samples, the analysed garnet porphyroblasts were selected among those showing the highest MnO content in the core, based on the MnO X-ray maps of the whole thin sections.

The bulk-rock compositions of each sample (i.e. measured bulk compositions: MBC; Table 2) were calculated combining the estimated mineral modes (Table 1) with mineral chemistry, and considering the molar volumes of each phase (details reported in the Supplementary Material, Tables SM2a-f). Mineral abbreviations in the text, figures and tables are from Whitney & Evans (2010).

3.2 Thermodynamic modelling

The P–T isochemical phase diagrams were calculated in the system MnNKCFMASTOH ($MnO–Na_2O–K_2O–CaO–FeO–MgO–Al_2O_3–SiO_2–TiO_2–Fe_2O_3–H_2O$), except for sample 17a-34, for which the system NKFMASTH was used, due to the lack of Mn-, Ca- and Fe^{3+}- bearing minerals. The pseudosections were calculated using Perplex 6.9.0 (version June 2020; Connolly, 1990, 2009) and the internally consistent thermodynamic dataset of Holland & Powell (1998, update 2004) (ds55). The following solution models were used: garnet, chloritoid, cordierite, staurolite and epidote (Holland & Powell, 1998), biotite (White et al., 2007), chlorite (Holland et al., 1998), feldspar (Fuhrman & Lindsley, 1988), white mica (Coggon & Holland, 2002; Auzanneau et al., 2010) and ilmenite (White et al., 2014). Quartz, kyanite/sillimanite and rutile were considered as pure phases.

Most of the modelled samples are graphitic phyllites; the occurrence of graphite should require, in principle, the use of a C-buffered COH equation of state (EoS) for fluid. However, in this study, fluid was treated in the more traditional way, using the EoS of Holland & Powell (1998) and assuming it is a saturated pure phase ($aH_2O = 1$). This choice is justified by considering that the finely dispersed graphite in these samples derives from the metamorphic recrystallization of the carbonaceous matter originally present in the sedimentary protoliths and it likely behaved as a passive phase during all the metamorphic evolution (i.e. neither it participated to fluid-rock interaction processes, nor it precipitated from the fluid). Tests conducted using the C-buffered COH EoS of Connolly & Cesare (1993) at $X(O)=0.333$ and $aC = 1$ (i.e. assuming an H_2O-dominated fluid in equilibrium with graphite) showed that the topology of the modelled phase diagrams does not change and that the shift of the phase assemblage boundaries is negligible ($\leq$ 10°C toward lower temperatures; see Supplementary Fig. SM2).

Five of the studied samples contain strongly zoned garnet porphyroblasts: for these samples, two P–T pseudosections were calculated considering the fractionation effects on the bulk composition due to the growth of the zoned garnets. The fractionated bulk compositions were obtained by subtracting the garnet core and mantle compositions (i.e. the modal amount of garnet core + mantle, as derived from the modal analysis of the X-ray maps) from the MBC. The two pseudosections were used to model: (i) the P-T conditions for the growth of garnet core and mantle (MBC, Table 2) and (ii) the P-T conditions for the growth of garnet rim in equilibrium with the matrix assemblage (MBC - garnet cores and mantles, Table 2). In both cases, P-T conditions were inferred based on the intersection of compositional isopleths modelled for garnet (core: GrtC; mantle: GrtM; rim: GrtR), biotite, staurolite, chlorite and plagioclase. Specifically, the intersection of XMn, XMg, XCa and XFe isopleths were used to constrain the P-T conditions of garnet growth, according to the following strategy: (i) the composition corresponding to the maximum XMn was selected for GrtC; (ii) an average composition was selected for GrtM; and (iii) the composition corresponding to the maximum XMg was considered for GrtR. The garnet isopleths intersection was defined considering an uncertainty of ± 0.01 for all the isopleths (e.g. Lanari & Duesterhoef, 2018). For biotite, staurolite and chlorite, the modelled XMg isopleths corresponding to the average measured XMg values were used, with uncertainties covering their compositional interval from the minimum to the maximum XMg. The same approach was applied to plagioclase, for which the XCa isopleths were used.

4. PETROGRAPHY AND MINERAL CHEMISTRY RESULTS

The studied samples are Al-rich metapelites, plotting above the garnet-chlorite tie line in the AFM diagram (Fig. 6e), with Mg/(Mg+Fe) values in the range 0.27–0.53. Three groups are identified, based on their bulk compositions: (1) samples with A ≥ 50 in both the AFM and ACF diagrams projected from muscovite ($A = Al_2O_3 - 3K_2O$); (2) samples with A<50 and very low MnO and CaO contents (MnO < 0.05 mol%; CaO < 1.0 mol%); (3) samples with A<50 and higher amounts of MnO and CaO (MnO>0.05 mol%; CaO>1.0 mol%). Group 1 includes samples 17a-34 and 17a-33, which are almost devoid of CaO and differ for the MnO content (null for 17a-34 and relatively high for 17a-33). Group 2 includes samples 17a-22 and 15a-15b, and Group 3 includes samples 15a-28b and 17a-42.

Most of the studied samples are garnet-bearing, two-micas ± chlorite phyllites; however, the most Al-rich samples (Group 1: 17a-34 and 17a-33) are almost devoid of biotite. Besides phyllosilicates, all the studied samples contain one or more of garnet, staurolite or kyanite, showing variable microstructural relationships with the main foliation. Blastesis-deformation relations for all the samples are reported in Fig. 7. In most samples, the peak assemblage consists of minerals (including garnet rim) statically overgrowing the main foliation (S_m); the development of the S_m is therefore ascribed to the prograde metamorphic stages. Early prograde and late prograde assemblages comprise those minerals that are inferred to be in equilibrium with garnet core and mantle, respectively. Sample 17a-34 differs from the others for the lack of garnet and of post-S_m minerals; the distinction between the late prograde and the peak assemblages is thus more uncertain.

4.1 Sample 17a-34

This kyanite–staurolite-bearing graphitic muscovitic schist consists of quartz (55%), muscovite (37%), chlorite (4%), kyanite (2%) and staurolite (2%), with accessory graphite and rutile. It shows a well-developed foliation (S_m) defined by the preferred orientation of muscovite (Si=3.05–3.10 a.p.f.u.), which is concentrated in mm-thick continuous layers alternated with discontinuous quartzitic layers of similar thickness. Staurolite (XMg=0.18–0.19) and kyanite occur as millimetric sized porphyroblasts wrapped around by the main foliation (i.e. pre-kinematic with respect to S_m) (Figs. 3a and 4a,b). They both include an internal foliation (S_{m-1}) mostly defined by quartz and graphite, and by minor chlorite and muscovite, discordant with respect to the external S_m (Fig. 4a,b). Staurolite is partially replaced at the rim by muscovite, and kyanite is locally overgrown by chlorite (Fig. 3a). Late fine-grained muscovite and medium-grained chlorite flakes overgrow statically the main foliation (i.e. they are post-kinematic with respect to the S_m).

4.2 Sample 17a-33

This garnet-bearing graphitic muscovitic schist consists of muscovite (80%), quartz (13%), biotite (4%) and garnet (2%), with rare staurolite and accessory ilmenite and graphite (Fig. 3b). The sample is characterized by a strong alteration, testified by the occurrence of abundant oxides and kaolinite. The main foliation S_m is defined by the preferred orientation of muscovite (Si=3.05–3.09 a.p.f.u.) and it is crenulated, with the development of a pervasive axial plane schistosity (S_{m+1}) defined by muscovite (Fig. 4c). Biotite is rare and mostly occurs as fine grained flakes statically overgrowing the S_m. The millimetric garnet porphyroblasts are wrapped around by the S_{m+1} and are likely in equilibrium with the S_m; they are almost free of inclusions, and are strongly oxidised at the rim and along fractures, where they are replaced by brownish-red Fe-oxides (Fig. 4c). Despite the strong oxidation at its rims, garnet preserves a prograde zoning, with XMn and XCa decreasing and XMg and XFe increasing towards the rim (Fig. 6a) (GrtC: XFe=0.75–0.78, XCa=0.025–0.035, XMg=0.095–0.13, XMn=0.07–0.12; GrtR: XFe=0.81–0.82, XCa=0.01–0.02, XMg=0.13–0.15, XMn=0.025–0.035). The S_m is overgrown by multi-mm aggregates of fine-grained kaolinite + Fe-oxide, this last being concentrated in the centre of the aggregates (Fig. 4d). These aggregates likely represent pseudomorphs after a former feldspar (e.g. plagioclase), post-kinematic with respect to the S_m. Staurolite is very rare (it has not been observed in the thin section used for mapping and compositional analysis); it forms mm-sized porphyroblasts overgrowing the S_m, but pre-kinematic with respect to the S_{m+1} (Fig. 4d). Among the accessory phases, fine-grained ilmenite is widespread in the matrix, where it is aligned with the S_m.

4.3 Sample 17a-22

This garnet–staurolite-bearing muscovite–chlorite schist consists of muscovite (47%), quartz (30%), chlorite (9%), plagioclase (5%), garnet (5%), biotite (2%), staurolite (1%) and accessory epidote, ilmenite and apatite. The main foliation (S_m) is defined by cm-thick phyllosilicate-rich layers alternated with mm-thick discontinuous quartzitic layers (Fig. 3c). The S_m is crenulated in gently open folds (Figs. 3c and 4e), without the development of an axial planar foliation. Muscovite (Si=3.06–3.12 a.p.f.u.) is the dominant phyllosilicate and it is aligned along the S_m; chlorite (XMg=0.51–0.55) and minor biotite (XMg=0.50–0.56) are mostly concentrated in pluri-millimetric continuous layers, in equilibrium with muscovite. Multi-mm sized garnet porphyroblasts are mostly syn-kinematic with respect to the S_m; they include a rotated internal foliation defined by inclusions of quartz, epidote and ilmenite, continuous with respect to the external S_m (Fig. 4e). Garnet shows a prograde zoning with XMn and XCa decreasing and XMg increasing rimward (Fig. 6a) (GrtC: XFe=0.71–0.75, XCa=0.14–0.17, XMg=0.06–0.08, XMn=0.015–0.06 and GrtM: XFe=0.75–0.78, XCa=0.12–0.14, XMg=0.10–0.12, XMn=0.00). Post-kinematic garnet rims, originally overgrowing the S_m, are completely replaced by a late generation of chlorite (Fig. 4f). Plagioclase (XAn=0.31–0.32) and staurolite (XMg=0.17–0.19) both occur as mm- to multi-mm sized porphyroblasts overgrowing the main foliation (post-S_m) (Fig. 4f). Among accessory phases, fine-grained epidote and ilmenite are both included in garnet and dispersed in the matrix, where they are aligned with the main foliation.

4.4 Sample 15a-15b

This two-mica, garnet–staurolite-bearing graphitic schist consists of muscovite (42%), quartz (38%), biotite (9%), garnet (5%), staurolite (2.5%), plagioclase (1%) and chlorite (1%), and accessory epidote, ilmenite, graphite and tourmaline. Its pervasive foliation (S_m) is defined by the preferred orientation of muscovite (Si=3.06–3.10 a.p.f.u.) and minor biotite (XMg=0.54–0.59), concentrated in pluri-mm continuous layers alternated with quartzitic layers of similar thickness (Figs. 3d and 5a). Muscovite occurs in two different generations: most of the fine-grained flakes are aligned parallel to the S_m (syn-S_m), but some flakes overgrowing the S_m are also observed (post-S_m). Also biotite occurs in syn-S_m and post-S_m generations; it is mostly fine-grained, although a few medium-grained porphyroblasts with a rotated internal foliation defined by graphite locally occur in the micaceous layers. Garnet porphyroblasts, up to several millimetres in size, are syn- to post- kinematic with respect to the S_m and preserve a typical growth zoning. The cores (GrtC: XFe=0.76–0.77, XCa=0.10–0.12, XMg=0.08–0.09, XMn=0.03–0.04) and mantles (GrtM: XFe=0.77–0.78, XCa=0.10-0.13, XMg=0.11-0.13, XMn=0.010-0.015) of garnet porphyroblasts, in fact, include a rotated internal foliation defined by the alignment of quartz and ilmenite inclusions (Fig. 5a), whereas their rims (GrtR: XFe=0.74–0.75, XCa=0.10–0.12, XMg=0.13–0.14, XMn=0.00) overgrow the S_m (Fig. 5b). Staurolite (XMg=0.19–0.21) occurs as mm-sized porphyroblasts syn- to post-kinematic with respect to the S_m. They either include an undulated internal foliation defined by quartz (Fig. 5c), or overgrow the S_m (Fig. 5d). Plagioclase (XAn=0.32) is scarce and forms mm-sized porphyroblasts statically overgrowing the S_m. Chlorite (XMg=0.53–0.54) is a late phase, mostly replacing garnet at its rim and rarely forming fine-grained flakes statically overgrowing the S_m (Fig. 3d). Epidote, ilmenite and tourmaline are both scattered within the matrix and included in garnet, where they define the internal foliation.

4.5 Sample 15a-28b

This two-mica, garnet–staurolite–kyanite-bearing schist consists of quartz (40%), muscovite (24%), garnet (21%), biotite (6%), chlorite (3%), kyanite (3%) and staurolite (2%), with accessory ilmenite and epidote. The main foliation (S_m) is marked by the preferred orientation of muscovite (Si=3.06–3.17), biotite (XMg=0.56–0.59) and minor chlorite (XMg=0.55–0.58), which define mm-thick continuous layers alternating with discontinuous quartzitic layers, and it is locally crenulated, with the development of open folds. The axial foliation (S_{m+1}) of these crenulation folds is only locally developed and it is mostly defined by muscovite and minor chlorite. The sample grain size is strongly heterogeneous for the presence of large garnet porphyroblasts, up to few cm in size, which preserve a prograde zoning (Fig. 3e). The cores of these garnet porphyroblasts are skeletal (Fig. 5e) and overgrow a S_{m-1} foliation, testified by the preserved shape of the microlithons and by the rare occurrence of muscovite and chlorite included in garnet. Garnet rims are idioblastic and statically overgrow the S_m foliation (i.e. post-S_m) (Fig. 5f,g), but predate the development of the crenulation. Due to the centimetric size of garnet, it is unlikely that the porphyroblasts have been cut through the real core; the measured GrtC composition is therefore referred to as the apparent garnet core composition (“GrtC”). Garnet (apparent) core, mantle and rim compositions are as follows, “GrtC”: XFe=0.68–0.70, XCa=0.18–0.19, XMg=0.08–0.09, XMn=0.03–0.04; GrtM: XFe=0.69–0.70, XCa=0.17–0.18, XMg=0.10–0.14, XMn=0.02–0.03; GrtR: XFe=0.71–0.72, XCa=0.14–0.15, XMg=0.13–0.14, XMn=0.00. Muscovite in the S_{m-1} is rarely preserved within garnet cores. In the matrix, muscovite occurs in two different generations: most of the fine-grained flakes define the S_m; a later generation statically overgrows the S_m and defines the S_{m+1}. Biotite and chlorite are less abundant than muscovite and mostly aligned with S_m; locally, few biotite flakes overgrowing the S_m also occur, and minor chlorite is aligned along the S_{m+1}. Both staurolite (XMg=0.17–0.20) and kyanite form mm-sized porphyroblasts (Fig. 5f,g). They occur in two generations: as inclusion in the garnet rim (i.e. late prograde phase) and in the matrix, where they statically overgrow the S_m (i.e. post-S_m). Epidote is rare and occurs as small idioblasts within the matrix and included in garnet core and mantle.

4.6 Sample 17a-42

This two-mica, garnet–kyanite-bearing graphitic schist consists of quartz (35%), muscovite (20%), garnet (16%), biotite (14%), kyanite (8%), plagioclase (6%) and minor chlorite with accessory ilmenite, apatite, epidote and rutile. The well-developed foliation (S_m) is defined by the preferred orientation of muscovite (Si=3.09–3.16 a.p.f.u.) and biotite (XMg=0.56–0.64), which form pluri-mm thick continuous layers alternated with mm-thick, discontinuous quartzitic layers (Fig. 3f). Both muscovite and biotite also occur as post-kinematic flakes, statically overgrowing the main foliation. Garnet occurs as multi-mm strongly zoned porphyroblasts characterized by two distinct growth zones. The core and mantle of these porphyroblasts include a rotated internal foliation (S_{m-1}) (Fig. 5h) mostly defined by quartz, epidote, ilmenite (in the core) and ilmenite + rutile (in the mantle); garnet cores (GrtC: XFe=0.66–0.69, XCa=0.18–0.21, XMg=0.07–0.10, XMn=0.02–0.06) and mantles (GrtM:

XFe=0.68–0.70, XCa=0.18–0.19, XMg=0.11–0.13, XMn=0.015–0.02) are interpreted as syn-S_{m-1}. They are surrounded by a thick rim (GrtR: XFe=0.69–0.71, XCa=0.16–0.18, XMg=0.13–0.15, XMn=0.00) statically overgrowing the main foliation and therefore interpreted as post-S_m (Fig. 5h,i); garnet rim includes quartz and rutile and is partially replaced by late chlorite. Multi-mm sized kyanite and plagioclase (XAn=0.34–0.47) porphyroblasts are both post-kinematic with respect to the S_m, statically overgrowing it (Fig. 5i,j). Rutile is widespread in the matrix, where it is partially replaced by ilmenite.

5. THERMODYNAMIC MODELLING RESULTS

The phase diagram approach (Figs. 8–10) was applied to all six metapelites in order to constrain their peak P-T conditions and to reconstruct their metamorphic evolution. The compositional isopleths with corresponding uncertainties are reported in Supplementary Figs. SM3-SM7; Supplementary Figs. SM8-SM12 show the complete unfractionated and fractionated P-T pseudosections calculated for each sample, whereas composite phase diagrams are presented in Figs. 8–10.

5.1 Sample 17a-34

Prograde evolution and development of S_m

The calculated P-T pseudosection shows that muscovite is stable over the whole P-T range of interest; chlorite is stable up to 560–610 °C at 5–12 kbar, and it is replaced by biotite at higher T. Kyanite is predicted over almost all the P-T range of interest, either in equilibrium with chloritoid (at T<520–580 °C) or with staurolite (at higher T). The garnet-in curve is located at P>11 kbar and T>630°C (Fig. 8a). Microstructural observations show that both staurolite and kyanite porphyroblasts are pre-kinematic with respect to the main foliation (Fig. 7a): thus, they provide information about the prograde evolution of the sample. Compositional isopleths modelled for staurolite (XMg=0.18 ± 0.01) constrain its growth at 575–590°C, P>8 kbar, in the Qz + Mu + Chl + St + Ky + Rt field (Fig. 8b,c and Supplementary Fig. SM3a), consistent with the observed prograde assemblage. The development of S_m should have occurred at higher T with respect to the growth of staurolite and kyanite, i.e. in the biotite stability field, according to the modelled pseudosection (Fig. 8a). Biotite is modelled in low amounts (<7 vol%); its absence in the sample could be justified by its replacement by chlorite during retrogression. This conclusion is supported by the observation that staurolite, and to a minor extent kyanite, are partially replaced by muscovite, thus confirming that the sample suffered a slight retrogression. The estimate of peak P-T conditions is hampered by the absence of preserved minerals post-kinematic with respect to the S_m (Fig. 7a).

5.2 Sample 17a-33

Prograde evolution and development of S_m

The pseudosection calculated for the unfractionated bulk composition (Fig. 8d and Supplementary Fig. SM8) shows that muscovite is stable over the entire P-T range of interest, in equilibrium with chlorite at T<560–600 °C, depending on pressure. The biotite-in curve has a positive slope, limiting its stability at T<560°C for P<6.5 kbar and at T>580°C for P>8.5 kbar. Garnet is predicted at T>510°C for P<9.5 kbar; however, its modal amount exceeds 0.5 vol% only at T>550°C, i.e. at a temperature which is 40° C higher than the garnet-in curve (Fig. 8f). Chloritoid is predicted at T<590°C and P>6.5 kbar, and is replaced by staurolite with increasing temperature. Staurolite is predicted to be stable up to 620–650°C; at higher T, it is replaced by kyanite. Plagioclase is limited to P<7.0–8.0 kbar. The compositional isopleths modelled for garnet core (GrtC: XMg=0.095, XCa=0.035, XMn=0.12, XFe=0.75; all with ± 0.01 uncertainties) are nearly parallel to each other (Fig. 8e and Supplementary Fig. SM3b), constraining its growth at T=550–570 °C and P>8.5 kbar, in the Qz + Mu + Chl + Grt + Ctd + Ilm field (Fig. 8f). The modelled amounts of chlorite and chloritoid at these P-T conditions are lower than 3 vol% and 2 vol%, respectively; thus, their absence from the observed prograde assemblage could be likely due to their complete consumption during prograde metamorphism.

The garnet porphyroblasts in their entirety (i.e. both GrtC and GrtR) are syn-kinematic with respect to the main foliation, i.e. they grew earlier than the metamorphic peak (Fig. 7b). The growth of the garnet rim is constrained using the P-T pseudosection calculated for the fractionated bulk composition. The effects of fractionation are minimal; the most significant variation concerns the position of the garnet-in curve, which is shifted up-T and up-P of about 50°C and 2 kbar, respectively, and the stability field of plagioclase, which is now enlarged toward higher P (Supplementary Fig. SM8). Compositional isopleths modelled for the garnet rim (GrtR: XMg=0.15, XCa=0.01, XMn=0.03, XFe=0.82; all with ± 0.01 uncertainties) converge at 585–595°C, 9.5–11.0 kbar (Fig. 8e,f and Supplementary Fig. SM3c). The absence of biotite in the main foliation constrains the development of the S_m at T<580–590°C, in equilibrium with garnet rim.

Peak P-T conditions

Peak P-T conditions are difficult to constrain, because the post-kinematic minerals overgrowing the main foliation are either completely altered (e.g. plagioclase is completely replaced by kaolinite, biotite is strongly oxidized) or very rare (e.g. staurolite), and were not found in the polished thin section used for compositional analysis. Both biotite and staurolite are predicted to be stable at temperatures higher than those estimated for the growth of GrtR, and plagioclase is modelled at P<8.0 kbar (Fig. 8d). Both these observations are consistent with a heating-decompression path, but peak metamorphic conditions cannot be more precisely constrained.

5.3 Sample 17a-22

Prograde evolution and development of S_m

The P-T pseudosection calculated for the unfractionated bulk composition (Fig. 9a and Supplementary Fig. SM9) shows that muscovite and biotite are stable in the whole P-T region of interest, whereas chlorite is stable at T<560–610 °C. The garnet-in curve is located at 500–530°C, and the 0.5 vol% garnet isomode is shifted up- T of 10°C (Fig. 9c); staurolite is modelled in the T interval of 560–640°C, and the staurolite-out curve mostly coincides with the kyanite-in curve. Na-bearing phases are paragonite and plagioclase, which are stable at low-T/high-P and high-T/low-P, respectively. The compositional isopleths modelled for garnet core (GrtC: XMg=0.06, XCa=0.17, XMn=0.06, XFe=0.72; all with ± 0.01 uncertainties) constrain its growth at 535–550°C and 5.5–6.0 kbar, in the Qz + Mu + Bt + Chl + Grt + Pl + Ilm ± Mt fields (Fig. 9b,c and Supplementary Fig. SM4). The modelled assemblage in equilibrium with garnet core is not consistent with the observed one; specifically, epidote is found as inclusion within GrtC, instead of plagioclase. This discrepancy will be discussed in section 6.1.

Both garnet core and garnet mantle are syn-kinematic with respect to the main foliation (Fig. 7c). Although the modelled XFe isopleths do not match perfectly with the observed GrtM composition (XFe=0.78 ± 0.01), the other compositional isopleths (GrtM: XMg=0.12, XCa=0.11, XMn=0.01; all with ± 0.01 uncertainties) converge at about 570–590°C and P>8.0 kbar, in the Qz + Mu + Bt + Chl ± Pg + Grt + Ilm fields (Fig. 9b,c and Supplementary Fig. SM4). With the exception of paragonite, whose amount is lower than 5 vol%, the modelled assemblage in equilibrium with GrtM is consistent with the observed one. Compositional isopleths of the syn-kinematic chlorite and biotite (Chl: XMg=0.53 ± 0.02; Bt: XMg=0.53 ± 0.03) constrain their growth at 560–580°C and 575–590°C, respectively, i.e. at conditions roughly overlapping with those estimated for garnet mantle (Fig. 9b,c). This implies that the S_m developed in the temperature interval of 570–590°C.

Peak P-T conditions

The P-T pseudosection calculated for the fractionated bulk composition shows that the effects of fractionation are minimal, and mostly reflected by a significant reduction of the garnet stability field, which is now limited at T>530–560°C (Supplementary Fig. SM9). As garnet rims are completely replaced by late chlorite, peak P-T conditions were constrained by the other post-kinematic minerals overgrowing the main foliation, i.e. staurolite and plagioclase. Compositional isopleths modelled for these phases (St: XMg=0.18 ± 0.01; Pl: XCa=0.31 ± 0.01) converge at 600–620°C and 8.0–9.0 kbar, constraining peak P-T conditions in the Qz + Mu + Bt + Grt + St + Pl + Ilm field, consistently with the observed peak assemblage (Fig. 9b,c and Supplementary Fig. SM4).

5.4 Sample 15a-15b

Prograde evolution and development of S_m

The P-T isochemical diagram calculated for the unfractionated bulk composition (Fig. 9d and Supplementary Fig. SM10) shows that muscovite is stable in the whole P-T range of interest, whereas chlorite is modelled at T<550–600 °C and is replaced by biotite at higher T. The garnet-in curve is located at ca. 510–530 °C, and the 0.5 vol% garnet isomode is shifted up-T of ca. 15–20°C (Fig. 9f). Chloritoid is stable at T<550–580°C and is replaced by staurolite at higher temperatures; kyanite is modelled at T>600°C. The plagioclase-in curve has a positive slope, constraining its stability at relatively low-P and high-T conditions. The intersection of the garnet core compositional isopleths (GrtC: XMg= 0.08, XCa= 0.11, XMn= 0.04, XFe=0.75;

all with ± 0.01 uncertainties) points to T = 550–565°C and P = 5.5–6.3 kbar for the growth of GrtC (in the Qz + Chl + Mu + Bt + Grt + St + Pl + Ilm field) (Fig. 9e and Supplementary Fig. SM5). For the garnet mantle, the modelled XFe isopleths do not match perfectly with the observed GrtM composition (XFe=0.77 ± 0.01); however, the other compositional isopleths (GrtM: XMg= 0.12, XCa= 0.11, XMn= 0.01; all with ± 0.01 uncertainties) converge at T=580–600°C and P=8.5–11.0 kbar (in the Qz + Chl + Mu ± Bt + Grt + St + Pl + Ilm fields) (Fig. 9f and Supplementary Fig. SM5). The observed mineral assemblage in equilibrium with GrtM (Qz + Mu ± Bt + Grt + St + Ilm) matches the field assemblages modelled for the growth of GrtM; on the opposite, the observed mineral assemblage in equilibrium with GrtC (Qz + Chl + Mu + Grt + Ep + Ilm) is not consistent with the plagioclase-bearing field modelled for the growth of GrtC (Fig. 9f). This discrepancy will be discussed in section 6.1.

Syn-kinematic biotite (Bt: XMg=0.57 ± 0.03) is predicted to form at the expenses of chlorite in the narrow T interval of 590–600°C, partially overlapping the P-T conditions predicted for the growth of GrtM (Fig. 9e,f and Supplementary Fig. SM5). This is in agreement with microstructural observations suggesting that GrtM is syn-kinematic with respect to the main foliation (Fig. 7d), and constrains the development of S_m at T<600°C.

Peak P-T conditions

The topology of the P-T pseudosection calculated for the fractionated bulk composition is similar to the unfractionated one, the main difference concerning the garnet stability field, now reduced to T>550°C and P>6.5 kbar (Supplementary Fig. SM10). The compositional isopleths of the post-kinematic garnet rim (GrtR: XMg=0.14, XCa=0.11, XMn=0, XFe=0.75; all with ± 0.01 uncertainties) constrain its growth at T=620–630°C, 8.4–8.7 kbar, in the Qz + Mu + Bt + Grt + St + Pl + Ky + Ilm field (Fig. 9e,f and Supplementary Fig. SM5). The predicted amount of kyanite in this field is <1 vol%. The compositional isopleths of the other post-kinematic phases in equilibrium with GrtR, i.e. staurolite, biotite and plagioclase (St: XMg=0.20 ± 0.01; Bt: XMg=0.57 ± 0.03; Pl: XCa=0.32 ± 0.01), intersect themselves in the slightly lower T interval of 600–625°C at 8.5–9.0 kbar (Fig. 9e,f and Supplementary Fig. SM5).

5.5 Sample 15a-28b

Prograde evolution and development of S_m

The P-T pseudosection calculated for the unfractionated bulk-composition (Fig. 10a and Supplementary Fig. SM11) shows that muscovite is stable in most of the P-T range of interest, in equilibrium with chlorite at T<530–600°C and with biotite at higher T. Garnet is stable over the whole P-T range of interest, the garnet-in curve being located at 440–470°C (i.e. outside the investigated P-T range; Fig. 10c), with the 0.5 vol% isomode shifted up-T of 15–20°C. Chloritoid is modelled up to 540–580°C, and at higher T it is replaced by staurolite. Kyanite is stable at T>580°C, and the kyanite-in curve mostly coincides with the staurolite-out curve. The compositional isopleths modelled for garnet apparent core (“GrtC”: XMg=0.08, XCa=0.185, XMn=0.04, XFe=0.69; all with ± 0.01 uncertainties) mutually intersect at 550–570 °C and >8.5 kbar, in the Qz + Mu + Chl + Grt + Ctd + Ep + Ilm field (Fig. 10b and

Supplementary Fig. SM6); this is consistent with the observed prograde assemblage, except for chloritoid which is predicted to occur in low amounts (<7 vol%) and could have been completely consumed during prograde metamorphism. The modelled isopleths for garnet mantle (GrtM: XMg=0.12, XCa=0.17, XMn=0.02, XFe=0.69; all with ± 0.01 uncertainties) constrain its growth at 570–590°C and 8.0–11.0 kbar, in the Qz + Mu + Chl + Grt + St ± Ep + Ilm fields (Fig. 10c and Supplementary Fig. SM6), in agreement with the occurrence of quartz, muscovite, chlorite, epidote and ilmenite inclusions in GrtM. The amount of staurolite predicted at these P-T conditions is lower than 3 vol%, and its absence as inclusion in GrtM is therefore justifiable. Both GrtC and GrtM are syn-kinematic with respect to the main foliation (Fig. 7e), defined by muscovite, chlorite and biotite. The modelled compositional isopleths for chlorite and biotite (Chl: XMg=0.57 ± 0.02; Bt: XMg=0.57 ± 0.02) suggest that chlorite grew at 565–575°C, and biotite appeared at slightly higher temperatures (T=590–600°C) (Fig. 10b,c and Supplementary Fig. SM6), thus constraining the development of S_m at 570–600°C.

Peak P-T conditions

The P-T pseudosection calculated for the fractionated bulk composition is used to constrain the growth of the garnet rim, in equilibrium with the other post-kinematic phases (i.e. biotite, staurolite and kyanite). The fractionation effects are significant (Supplementary Fig. SM11); the garnet-in curve is now located at T>560°C, and the staurolite and kyanite stability fields are enlarged toward higher P and lower T, respectively. Compositional isopleths modelled for the garnet rim (GrtR: XMg=0.14, XCa=0.15, XMn=0, XFe=0.72; all with ± 0.01 uncertainties) constrain its growth at T=615–625°C and P=7.8–8.5 kbar, in the Qz + Mu + Bt + Grt + Ky + St + Pl + Ilm ± Mt fields (Fig. 10b,c and Supplementary Fig. SM6), in agreement with the observed peak metamorphic assemblage (plagioclase is predicted in very low amounts, <1 vol%). Compositional isopleths of staurolite (St: XMg=0.19 ± 0.02) suggest that this phase grew at 600–620°C (Fig. 10b,c and Supplementary Fig. SM6), consistent with the occurrence of post-kinematic staurolite in equilibrium with garnet rim.

5.6 Sample 17a-42

Prograde evolution and development of S_m

The pseudosection calculated for the unfractionated bulk-composition (Fig. 10d and Supplementary Fig. SM12) shows that muscovite is stable in almost all the P-T range of interest, either in equilibrium with chlorite (at T<560–610 °C)) or with biotite (at higher T). The garnet-in curve is located at T<530°C, and the 0.5 vol% garnet isomode is shifted up-T of 10–15°C (Fig. 10f); chloritoid is modelled up to 550–580°C and is replaced by staurolite at higher T, and kyanite is stable at T>580°C for P>11 kbar, and at T>600°C for P<8 kbar. The plagioclase-in curve has a positive slope, constraining its stability at relatively low-P and high-T conditions. The compositional isopleths modelled for the garnet core (GrtC: XMg=0.07, XCa=0.21, XMn=0.06, XFe=0.67; all with ± 0.01 uncertainties) converge at 535–555 °C and 7.0–9.2 kbar, in the Qz + Mu + Chl + Grt + Ctd + Ep + Ilm fields (Fig. 10e,f and Supplementary Fig. SM7). Except for chloritoid, which is nevertheless a minor phase (<3 vol%), the modelled assemblage is consistent with the observed inclusions in GrtC (e.g. epidote and ilmenite). Compositional isopleths modelled for the garnet mantle (GrtM: XMg=0.12, XCa=0.18, XMn=0.015, XFe=0.69; all with ± 0.01 uncertainties) converge at 570–590 °C and 9.0–11.0 kbar, in the Qz + Mu + Chl + Grt + St + Ep + Ilm + Rt field (Fig. 10e,f and Supplementary Fig. SM7); the coexistence of ilmenite and rutile in this field is in good agreement with microstructural observations (i.e. inclusions of both ilmenite and rutile in GrtM; Fig. 7f). The isopleths modelled for the syn-kinematic biotite (XMg=0.60 ± 0.04) allow constraining the development of the S_m at about 600–620°C, i.e. at higher T with respect to the growth of GrtM, consistently with the pre-kinematic (pre-S_m) nature of GrtC and GrtM.

Peak P-T conditions

The peak assemblage, represented by the post-kinematic garnet rim, kyanite, plagioclase, biotite and muscovite, is modelled by the pseudosection calculated using the fractionated bulk composition. The most significant effects of fractionation are represented by the shift of garnet-in curve up-T of about 40°C, and by the enlargement of the staurolite and kyanite stability fields toward higher P and lower T, respectively (Supplementary Fig. SM12). Compositional isopleths modelled for garnet rim (GrtR: XMg= 0.14, XCa= 0.17, XMn= 0.00, XFe=0.70; all with ± 0.01 uncertainties) constrain its growth at 610–625°C and 8.0–8.6 kbar, in the Qz + Mu + Bt + Grt + Ky + Pl + Ilm field (Fig. 10e,f and Supplementary Fig. SM7), which is consistent with the observed peak assemblage. Compositional isopleths modelled for plagioclase (XCa= 0.40 ± 0.06) are partially overlapped with those of GrtR, thus defining peak P-T conditions of 600–635°C and 8.4–9.5 kbar (Fig. 10e,f and Supplementary Fig. SM7).

6. DISCUSSION

6.1 Equilibrium vs. kinetic -controlled growth of garnet core

The isochemical phase diagram approach is based on the principles of equilibrium thermodynamics, i.e. on the assumption that each mineral grew in equilibrium with its surroundings, and thus its composition reflects the predicted P-T conditions (e.g. Guiraud et al., 2001; Powell et al., 2005; Powell & Holland, 2008). However, this assumption is not always valid for garnet porphyroblasts, which often nucleate and grow only after significant overstepping of the garnet-in curve, i.e. at higher T and/or P conditions with respect to those predicted by equilibrium thermodynamics (Hollister, 1969; Waters & Lovegrove, 2002; Pattison & Tinkham, 2009; Spear et al., 2014; Carlson et al., 2015; Castro & Spear, 2016; Wolfe & Spear, 2018; Spear & Wolfe, 2018; Nagurney et al., 2021).

The results of our thermodynamic modelling show that, for all the garnet-bearing samples, the P-T conditions inferred for garnet nucleation do not match the garnet-in reaction modelled by the pseudosections, but lie at higher temperatures with respect to the garnet-in curve. We interpret this as evidence of temperature-overstepping of garnet nucleation, with degree of overstepping varying from 10–15 °C for samples 17a-22 and 15a-15b, to 20 °C for sample 17a-42, 40 °C for sample 17a-33, and more than 50 °C for sample 15a-28b (Fig. 11c-g). Our results also show that, with the exception of sample 15a-28b, the modelled GrtC compositional isopleths systematically define P-T conditions lying on (or close to) the modelled 0.5% isomodes (Fig. 11c,e-g). Sample 15a-28b differs from the others because, at the P-T conditions defined by "GrtC" isopleths intersection, the predicted garnet abundance is significantly higher (14%) than in the other samples. This is likely due to our failing in sectioning the centimetric sized porphyroblasts through the real core (i.e. the measured composition of "GrtC" does not reflect the composition of the first garnet nucleus).

Comparing the P-T conditions constrained for the growth of GrtC with the assemblages predicted to be stable at the same conditions, we note:

(i) for two samples (17a-22 and 15a-15b), the P-T conditions constrained for the growth of GrtC lie in fields which are not consistent with the observed assemblages in equilibrium with GrtC. Specifically, in both samples, the estimated P-T conditions are located at pressures which are lower than those predicted for the early prograde assemblages (Fig. 9c,f). Also, the prograde P-T paths defined for these two samples based on the P-T conditions estimated for GrtC and GrtM suggest nearly isothermal loading (<10 °C kbar^{-1}), which is anomalous in the context of Barrovian terranes (e.g. Gaidies et al., 2015). The discrepancy between the modelled and the observed early prograde assemblages, as well as the anomalous sub-vertical prograde paths suggest that garnet nucleation probably occurred after a significant pressure-overstepping, i.e. at pressures at least 2–3 kbar higher than those predicted by the pseudosections;

(ii) for the other three garnet-bearing samples (17a-33, 15a-28b and 17a-42), the growth of GrtC is predicted to occur in fields which are consistent with the observed early prograde mineral assemblages (Figs. 8f and 10c,f). Their prograde P-T paths calculated in the same way as in the previous samples display heating associated to a moderate loading (>25 °C kbar^{-1}), i.e. a typical scenario in Barrovian terranes (e.g. Gaidies et al., 2015). This suggests that, in these samples, the degree of pressure-overstepping (if any) was minimal.

Overall, these results support the conclusions of previous studies (e.g. Carlson et al., 2015; Spear & Wolfe, 2019 and references therein), confirming that garnet nucleation can be influenced by kinetic factors. To explore which parameters may be responsible for the delay in garnet appearance with respect to the equilibrium predictions, we considered the difference in bulk composition among the samples, with specific emphasis on MnO and CaO:

(i) bulk-rock MnO: previous studies demonstrated that samples with higher bulk-rock MnO content generally display more pronounced apparent overstepping of the garnet-in reaction (Nagurney et al., 2021). Our results confirm this conclusion, i.e. the samples with higher MnO content normalized to FeO+MgO+MnO (samples from Groups 1 and 3: 17a-33, 17a-42 and 15a-28b) are those for which garnet nucleation was apparently more overstepped toward higher temperatures (Fig. 11a). However, the apparent delay in garnet nucleation coincides with the temperature difference between the modelled garnet-in curve and the 0.5% isomode (Fig. 11c-f). This suggests that the T-overstepping of the garnet-in reaction could have been negligible for all the samples, and that the apparent delayed garnet nucleation could reflect the attainment of the critical 0.5% threshold of garnet abundance, below which garnet is not readily detected in thin section (see also Nagurney et al., 2021 for a similar conclusion).

(ii) bulk-rock CaO: we note that, in the two samples showing discrepancies between calculated and observed assemblages in equilibrium with GrtC (samples 17a-22 and 15a-15b), the main cause of discrepancy is related to the location of the grossular isopleths (Fig. 9b,e). This observation is in line with the conclusions of Spear & Wolfe (2019), who demonstrated that the net transfer equilibrium controlling the grossular content in garnet is the one which is more influenced in case of overstepping. Although we recognise that the number of investigated samples is small, the two samples with lower bulk-rock CaO content (samples from Group 2: 17a-22 and 15a-15b) are those displaying the largest evidence of P-overstepping (sample 17a-33 is not considered here because it can be fundamentally described in a CaO-free system) (Fig. 11b,f,g).

We therefore suggest that the T-overstepping of garnet nucleation was likely mostly influenced by the bulk-rock MnO content, i.e. the higher the bulk-rock MnO content, the more pronounced the apparent ΔT overstepping (Fig. 11a), whereas the P-overstepping of the garnet-in reaction was likely influenced by the bulk-rock CaO, i.e. the lower the bulk-rock CaO content, the more pronounced the ΔP overstepping (Fig. 11b). Based on the results of forward thermodynamic modelling, overstepping nucleation of garnet should be presumed if the P-T conditions defined by garnet core lie at temperatures higher than the modelled garnet-in reaction, and if: (i) there are incongruities between the assemblage predicted to be stable at these P-T conditions and the assemblage observed in equilibrium with garnet core (see also Carlson et al., 2015 and references therein), and (ii) an anomalous nearly isothermal loading path is inferred. In such a case, the prograde P-T conditions inferred from garnet core composition should be considered with suspicion, because significant P-overstepping (rather than T-overstepping) of garnet nucleation could have occurred.

Kinetic factors seem instead much less critical in controlling the growth of the garnet rim at peak P-T conditions, as previously demonstrated by Spear & Wolfe (2019). For all the investigated samples, in fact, the modeled peak assemblages and mineral compositions are in good agreement with the observed ones and point to peak P-T conditions which are consistent among the samples. This confirms that the assumption of garnet rim growing in equilibrium with the surrounding matrix is reasonable, and that peak metamorphic conditions constrained through equilibrium approaches based on the composition of garnet rim and of the matrix assemblage can be considered as reliable.

6.2 P-T evolution of the Upper-LHS: regional implications and methodological considerations

In all the samples, the compositional isopleths used to constrain the prograde P-T conditions are mostly T-dependent and parallel to each other, providing tight constraints on temperature, but poor constraints on pressure. Peak P-T conditions are, instead, well constrained for most of the samples because they are defined based on low-variant assemblages. In spite of the relatively large uncertainties on the estimated prograde pressures, all the reconstructed P-T paths show a common shape, characterized by a prograde moderate increase in both P and T, up to peak-P conditions, followed by a heating decompression, up to peak-T conditions (Fig. 12). Peak-P conditions are invariably reached at T=580–590°C in all the samples, spanning 8.5–11 kbar. Considering that all the samples belong to the Upper-LHS unit and should therefore have experienced the same P-T evolution, this range can be reduced to 9.5–10.5 kbar by overlapping all the trajectories. Peak-T conditions are tightly constrained at 610–630 °C and 8.2–8.9 kbar, and are consistent among the samples (Fig. 12). The development of the main foliation is constrained at 580–600°C, earlier than the static growth of minerals defining the peak assemblage (Fig. 12).

These results show that, in the study area, the Upper-LHS experienced the temperature peak after the pressure peak, in agreement with the P-T paths reported westward by Catlos et al. (2001) and Kohn et al. (2001) (Margsyandi and Daraundi sections, central Nepal; their Domain 3) (see also Kohn, 2014 and Catlos et al., 2018), and eastward by Groppo et al. (2009), Mosca et al. (2012) and Rolfo et al. (2015) (Arun and Tamor sections, eastern Nepal; their Lower MCTZ or Lower IMS units). This type of P-T trajectory is significantly different from the hairpin P-T path generally described for the Lower-LHS unit, which is characterized by maximum temperature experienced at maximum pressure (e.g. Catlos et al., 2001; Kohn et al., 2001; Groppo et al., 2009; Imayama et al., 2010; Mosca et al., 2012; Rolfo et al., 2015; Rapa et al., 2016, 2018). The occurrence of P-T paths with different shapes in the Lower- and Upper- LHS units has been explained by previous authors (Catlos et al., 2001, 2018; Kohn et al., 2001) as the result of the accretion of different LHS tectonic slices to the MCT hanging wall, through a progressive southward (and downward) propagation of the thrust activity. According to this model, during the evolution of the MCT in early Miocene, the Upper-LHS rocks in the footwall experienced an increase in both P and T during tectonic loading. The successive slowdown (or quiescence) of the movement along the MCT allowed isotherms to relax and temperature to increase in the Upper-LHS unit, at slightly decreasing pressure and in the absence of significant deformation. The reactivation of strain occurred through the downward propagation of the thrust, which allowed the contemporaneous exhumation of the Upper-LHS unit and the burial of the Lower-LHS unit. Our results strongly support this model; in particular, the static growth of the main minerals defining the peak assemblages documented in this study provides strong evidence that decompression coupled with heating occurred in the absence of deformation, i.e. in the time interval between two episodes of intense thrusting.

One may wonder why this type of P-T trajectory has rarely been reported so far from the Upper-LHS in Nepal Himalaya. In our opinion, this may be due to:

(i) the substantial lack of studies based on forward petrological modelling. Most studies focusing on the LHS metamorphic evolution are based on inverse thermodynamic modelling approaches, i.e. conventional and/or multi-equilibrium thermobarometry (e.g. Macfarlane, 1995; Rai et al., 1998; Catlos et al., 2001; Kohn et al., 2001; Goscombe et al., 2006, 2018; Kohn, 2008; Groppo et al., 2009; Martin et al., 2010; Imayama et al., 2010; Corrie & Kohn, 2011; Mosca et al., 2012; Rolfo et al., 2015; Rapa et al., 2016, 2018; Khanal et al., 2020). These methods require the precise knowledge of the composition of minerals supposed to be in equilibrium at a certain metamorphic stage (e.g. garnet-biotite pair for the Grt-Bt thermometer; all the minerals defining a specific assemblage for Average PT etc.). While the peak assemblage in common metapelites is typically well preserved and often consists of several minerals (i.e. it is a low-variant assemblage), the prograde assemblages are more difficult to be defined, because some minerals stable during the prograde stages may have been consumed or may have changed their composition during the prograde evolution. For this reason, the inverse modelling approaches have been mostly applied to the peak assemblages, but not to the prograde assemblages, thus hampering the reconstruction of the whole P-T paths. Forward modelling approaches, i.e. isochemical phase diagrams combined with isopleth thermobarometry, allow this issue to be overcome; with this method, in fact, prograde P-T conditions can be constrained basing on the composition even of a single mineral (typically garnet), combined with the predicted stability field of the inferred prograde assemblages.

(ii) the relatively rare occurrence, in the LHS, of appropriate lithologies for documenting the static growth of the low-variant peak metamorphic assemblage, and especially of the garnet rim. It is well known that deformation enhances metamorphic reactions (e.g. Terry & Heidelbach, 2006); in the absence of deformation, however, mineral growth is mostly controlled by diffusion, and metamorphic reactions are dependent on the bulk composition (Carlson, 1989; Ketcham & Carlson, 2012). It is therefore expected that significant growth (i.e. growth in amounts which can be easily detectable under the microscope) of aluminous minerals such as garnet, staurolite and kyanite (i.e. minerals commonly used as thermobarometers) is favoured by high-Al bulk compositions. Al-rich metapelites, whose composition plots above the garnet-chlorite tie line in the AFM diagram, are, therefore, the most suitable candidates for recording the peak metamorphic stage. Conversely, the heating decompression stage might remain elusive and/or difficult to be constrained in low-Al metapelites.

(iii) the still controversial definition of the MCT. The consequent uncertainties in the exact location of the MCT (see Section 2) lead to ambiguities in what is to be considered as Upper-LHS and what is instead Lower-GHS, so that a same litho-stratigraphic unit can have been placed alternatively in the Upper-LHS or in the Lower-GHS depending on the criteria adopted by different authors (see Searle et al., 2008 for further discussion).

Following these considerations, we suggest that the ideal approach for a detailed reconstruction of the whole P-T evolution of the Upper-LHS is to apply the thermodynamic forward modelling approach on Al-rich metapelites (see also Catlos et al., 2018, 2020 for a similar strategy), especially looking for those samples that show microstructural evidences of static growth of the main peak mineral phases. However, recognizing the evidence of overstepping garnet nucleation is important for the definition of the correct prograde path. The application of this method on a suite of samples from the same unit (rather than on a single sample) can be helpful in this sense.

7. CONCLUSIONS

In this paper, our detailed microstructural, petrographic and P-T forward modelling study of aluminous metapelites from the Upper-LHS of central Nepal supports the following conclusions:

(1) All the investigated samples experienced different degrees of apparent overstepping of garnet nucleation. The P-T conditions inferred for the growth of garnet cores lie at higher temperatures with respect to the modelled garnet-in reaction (apparent thermal, ΔT, overstepping), and/or at lower pressures compared to the early prograde assemblages predicted by the pseudosections (apparent baric, ΔP, overstepping). We suggest that the different degrees of the apparent ΔT and ΔP overstepping of the garnet-in reaction were influenced by bulk-rock compositional factors. ΔT overstepping is positively correlated with the bulk-rock MnO content; however, the apparent ΔT overstepping could reflect the attainment of the critical 0.5% threshold of garnet mode, rather than an effective delay of garnet appearance with respect to equilibrium predictions (see also Nagurney et al., 2021 for a similar conclusion). ΔP overstepping is negatively correlated with the bulk-rock CaO content (in agreement with what observed by Spear & Wolfe, 2019), and should be presumed if there are incongruities between the modelled and the observed assemblages and if an anomalous nearly isothermal loading path is inferred.

(2) The growth of the garnet rim at peak P-T conditions is not significantly influenced by kinetic factors, confirming that peak metamorphic conditions constrained through equilibrium approaches based on the composition of garnet rim and of the matrix assemblage can be considered as reliable (see also Spear & Wolfe, 2019).

(3) The P-T paths inferred for the Upper-LHS samples are characterised by prograde heating coupled with tectonic overload up to peak-P conditions of 9.5–10.5 kbar and 580–590°C, followed by heating during exhumation at peak-T conditions of 8.2–8.9 kbar and 610–630 °C. These results, combined with the observed static growth of the main minerals defining the peak assemblages, provide strong evidence that decompression coupled with heating occurred in the absence of deformation, thus supporting those thermo-mechanical models that predict a period of slowdown (or quiescence) of the Main Central Thrust activity.

ACKNOWLEDGEMENTS

The studied samples were collected during two field campaigns in central Nepal, which were funded by the Italian Ministry of University and Research (PRIN2010–2011, Project n°: 2010PMKZX7; PRIN2015, Project n°: 015EC9PJ5) and by the Compagnia di San Paolo and University of Torino (Junior PI Grant, Project n°: TO_Call1_2012_0068). Laboratory work was funded by the Italian Ministry of University and Research (PRIN 2017, Project n°: 2017LMNLAW) and by the University of Torino (Ricerca Locale, ex-60% 2020 funds: ROLF_RILO_20_01). We thank A. Nagurney for her inspiring and constructive comments, an anonymous reviewer for the helpful review, and C. Warren for helpful suggestions and editorial handling, which all significantly improved this work.

DATA AVAILABILITY

The data that supports the findings of this study are available in the Supplementary Material of this article.

SUPPORTING INFORMATION

Additional supporting information may be found in the online version of the article at the publisher's website.

Mineral chemistry results: this section includes the description of the mineral chemistry results, less condensed than that reported in the main text.

Figure SM1: Compositional profiles of representative garnet porphyroblasts.

Figure SM2: P–T pseudosections modelled for samples 17a-34 and 17a-42 using the C-buffered COH EoS of Connolly & Cesare (1993) at X(O)=0.333 and aC = 1 (i.e. assuming an H_2O-dominated fluid in equilibrium with graphite).

Figures SM3-SM7: P–T pseudosections modelled for the studied samples, contoured with the compositional isopleths of the main mineral phases, each one represented with the correspondent uncertainties.

Figures SM8-SM12: P–T pseudosections modelled for the garnet-bearing samples using the unfractionated and fractionated bulk compositions.

Table SM1: Excel spreadsheets reporting the whole set of compositional data for all the minerals analysed in the studied samples.

Table SM2: Excel spreadsheets used to calculate the bulk rock compositions combining the estimated mineral modes with mineral chemistry, and considering the molar volumes of each phase.

REFERENCES

Auzanneau, E., Schmidt, M. W., Vielzeuf, D., & Connolly, J.A.D. (2010). Titanium in phengite: a geobarometer for high temperature eclogites. *Contributions to Mineralogy and Petrology*, *159*, 1–24.

Carlson, W. D. (1989). The significance of intergranular diffusion to the mechanisms and kinetics of porphyroblast crystallization. *Contributions to Mineralogy and Petrology*, *103*, 1–24.

Carlson, W. D., Pattison, D. R. M., & Caddick, M. J. (2015). Beyond the equilibrium paradigm: How consideration of kinetics enhances metamorphic interpretation. *American Mineralogist, 100*, 1659–1667.

Castro, A. E., & Spear, F. S. (2016). Reaction overstepping and re-evaluation of peak P-T conditions of the blueschist unit Sifnos, Greece: implications for the Cyclades subduction zone. *International Geology Review, 59*, 548–562.

Catlos E. J., Lovera, O. M., Kelly, E. D., Ashley, K. T., Harrison, T. M., & Etzel, T. (2018). Modeling High-Resolution Pressure-Temperature Paths Across the Himalayan Main Central Thrust (Central Nepal): Implications for the Dynamics of Collision. *Tectonics, 37*, 2363–2388.

Catlos, E. J., Harrison, T. M., Grove, M., Ryerson, F. J., Manning, C. E., & Upreti, B. N. (2001). Geochronologic and thermobarometric constrains on the evolution of the Main Central Thrust, central Nepal Himalya. *Journal of Geophysical Research, Solid Earth, 106*, 16177–16204.

Catlos, E. J., Perez, T. J., Lovera, O. M., Dubey, C. S., Schmitt, A. K., & Etzel, T. M. (2020). High-resolution P-T-Time paths across himalayan faults exposed along the bhagirathi transect NW India: Implications for the construction of the Himalayan orogen and ongoing deformation. *Geochemistry, Geophysics, Geosystems, 21*, e2020GC009353.

Coggon, R., & Holland, T. J. B. (2002). Mixing properties of phengitic micas and revised garnet-phengite thermobarometers. *Journal of Metamorphic Geology*, *20*, 683–698.

Connolly, J. A. D., & Cesare B. (1993). C–O–H–S fluid compositions and oxygen fugacity in graphitic metapelites. *Journal of Metamorphic Geology, 11*, 379–388

Connolly, J. A. D. (1990). Multivariable phase diagrams: an algorithm based on generalize thermodynamics. *American Journal of Science, 290*, 666–718.

Connolly, J. A. D. (2009). The geodynamic equation of state: what and how. *Geochemistry, Geophysics, Geosystems, 10*, Q10014.

Corrie, S. L., & Kohn, M. J. (2011). Metamorphic history of the central Himalaya, Annapurna region, Nepal, and implications for tectonic models. *Geological Society of America Bulletin, 123*, 1863–1879.

DeCelles P. G., Gehrels G. E, Quade J., & Ojha T.P. (2000). Eocene-early Miocene foreland basin development and the history of Himalayan thrusting, western and central Nepal. *Tectonics, 17*, 741–765.

Dhital, M. R. (2015). Geology of Nepal Himalaya. Regional perspective of the classic collided orogen. Regional Geology Review. Springer International Publishing Switzerland, 498 pp.

Fuhrman, M. L. & Lindsley, D. H. (1988). Ternary-feldspar modeling and thermometry. *American Mineralogist, 73*, 201–215.

Gaidies, F., & George, F. R. (2021). The interfacial energy penalty to crystal growth close to equilibrium. *Geology, 49*, 988–992.

Gaidies, F., Krenn, E., De Capitani, C., & Abart, R. (2008). Coupling forward modelling of garnet growth with monazite geochronology: An application to the Rappold Complex (Austroalpine crystalline basement). *Journal of Metamorphic Geology, 26*, 775–793.

Gaidies, F., Petley-Ragan, A., Chakraborty, S., Dasgupta, S., & Jones, P. (2015). Constraining the conditions of Barrovian metamorphism in Sikkim, India: P-T-t paths of garnet crystallization in the Lesser Himalayan Belt. *Journal of Metamorphic Geology, 33*, 23–44.

Gansser, A. (1964). Geology of the Himalayas. Interscience, John Wiley and Sons, London, 289 pp.

George, F. R., & Gaidies, F. (2017). Characterisation of a garnet population from the Sikkim Himalaya: Insights into the rates and mechanisms of porphyroblast crystallisation. *Contributions to Mineralogy and Petrology, 172*, 1–22.

Goscombe, B., Gray, D., & Foster, D. A. (2018). Metamorphic response to collision in the Central Himalayan Orogen. *Gondwana Research, 57*, 191–265.

Goscombe, B., Gray, D., & Hand, M. (2006). Crustal architecture of the Himalayan metamorphic front in eastern Nepal. *Gondwana Research, 10*, 232–255.

Groppo, C., Rolfo, F. & Mosca, P. (2013). The cordierite-bearing anatectic rocks of the Higher Himalayan Crystallines (eastern Nepal): low-pressure anatexis, melt-productivity, melt loss and the preservation of cordierite. *Journal of Metamorphic Geology, 31*, 187–204.

Groppo, C., Rolfo, F., & Indares, A. (2012). Partial melting in the Higher Himalayan Crystallines of Eastern Nepal: the effect of decompression and implications for the “channel flow” model. *Journal of Petrology, 53*, 1057–1088.

Groppo, C., Rolfo, F., & Lombardo, B. (2009). P-T evolution across the Main Central Thrust Zone (Eastern Nepal): hidden discontinuities revealed by petrology. *Journal of Petrology, 50*, 1149–1180.

Groppo, C., Rubatto, D., Rolfo, F., & Lombardo, B. (2010). Early Oligocene partial melting in the Main Central Thrust Zone (Arun Valley, eastern Nepal Himalaya). *Lithos, 118*, 287–301.

Guiraud, M., Powell, R. & Rebay, G. (2001). H_2O in metamorphism and the preservation of metamorphic mineral assemblages. *Journal of Metamorphic Geology, 19*, 445–454

He, D., Webb, A. A. G., Larson, K. P., Martin, A. J., & Schmitt, A.K. (2015). Extrusion cs. Duplexing models of Himalayan Mountain building. 3: duplexing dominants from the Oligocene to Present. *International Geology Review, 57*, 1–27.

Holland, T., Baker, J., & Powell, R. (1998). Mixing properties and activity-composition relationships of chlorites in the system $MgO\text{-}FeO\text{-}Al_2O_3\text{-}SiO_2\text{-}H_2O$. *European Journal of Mineralogy, 10*, 395–406

Holland, T. J. B., & Powell, R. (1998). An internally consistent thermodynamic data set for phases of petrologic interest. *Journal of Metamorphic Geology, 16*, 309–343.

Hollister, L. S. (1969). Metastable paragenetic sequence of andalusite, kyanite, and sillimanite, Kwoiek Area, B.C. *American Journal of Science, 267*, 352–370.

Imayama, T., Takeshita, T., & Arita, K. (2010). Metamorphic P-T profile and P–T path discontinuity across the far-eastern Nepal Himalaya: investigation of channel flow models. *Journal of Metamorphic Geology*, *28*, 527–549.

Ketcham, R. A. & Carlson, W. D. (2012). Numerical simulation of diffusion-controlled nucleation and growth of porphyroblasts. *Journal of Metamorphic Geology*, *30*, 489–512.

Khanal, G. P., Wang J. M., Wu F. Y., Wang J. G., & Yang L. (2020). In-sequence buoyancy extrusion of the Himalayan Metamorphic Core, central Nepal: Constraints from monazite petrochronology and thermobarometry. *Journal of Asian Earth Sciences, 199*, 104406.

Kohn, M. J., Catlos, E. J., Ryerson, F. J., & Harrison, T. M. (2001). Pressure-temperature-time path discontinuity in the Main Central thrust zone, central Nepal*. Geology, 29*, 571–574.

Kohn, M. J., Paul, S. K., & Corrie, S. L. (2010). The lower Lesser Himalayan sequence: a Paleoproterozoic arc on the northern margin of the Indian plate. *Geological Society of America Bulletin, 122*, 323–335.

Kohn, M. J. (2008). PTt data from central Nepal support critical taper and repudiate large-scale channel flow of the Grater Himalayan Sequence. *Geological Society of America Bulletin, 120*, 259–273.

Kohn, M.J. (2014). Himalayan metamorphism and its tectonic implications. *Annual Review of Earth and Planetary Sciences, 42*, 381–419.

Kohn, M. J., Wieland, M. S., Parkinson, C. D., & Upreti, B. N. (2004). Miocene faulting at plate tectonic velocity in the Himalaya of central Nepal. *Earth and Planetary Science Letters, 228*, 299– 310.

Lanari, P., & Duesterhoeft, E. (2019). Modeling metamorphic rocks using equilibrium thermodynamics and internally consistent databases: Past achievements, problems and perspectives. *Journal of Petrology, 60,* 19–56.

Larson, K. P., Cottle, J. M., Lederer, G., & Rai, S. M. (2017). Defining shear zone boundaries using fabric intensity gradients: an example from the East-Central Nepal Himalaya. *Geosphere, 13,* 771–781

Larson, K. P., Piercey, S., & Cottle, J. (2019). Preservation of a Paleoproterozoic rifted margin in the Himalaya: insight from the Ulleri-Phaplu-Melung orthogneiss. *Geoscience Frontiers, 10*, 873-883.

Macfarlane, A. M. (1995). An evaluation of the inverted metamorphic gradient at Langtang National Park, central Nepal Himalaya. *Journal of Metamorphic Geology, 13*, 595–612.

Martin, A. J., Ganguly, J., DeCelles, P. G. (2010). Metamorphism of Greater and Lesser Himalayan rocks exposed in the Modi Khola valley, central Nepal. *Contribution to Mineralogy and Petrology, 159*, 203–223.

Martin, A. J., Burgya, K. D., Kaufmanb, A. J., & Gehrels, G. E. (2011). Stratigraphic and tectonic implications of field and isotopic constraints on depositional ages of Proterozoic Lesser Himalayan rocks in central Nepal. *Precambrian Research, 185*, 1–17.

Martin, A. J., DeCelles, P. G., Gehrels, G. H., Patchett, P. J., & Isachsen, C. (2005). Isotopic and structural constraints on the location of the Main Central Thrust in the Annapurna Range, central Nepal Himalaya. *Geological Society of America Bulletin, 117*, 926–944.

Montomoli, C., Iaccarino, S., Carosi, R., Langone, A., & Visonà, D. (2013). Tectonometamorphic discontinuities within the Greater Himalayan Sequence in Western Nepal (Central Himalaya): Insights on the exhumation of crystalline rocks. *Tectonophysics, 608*, 1349–1370.

Mosca, P., Groppo, C., & Rolfo, F. (2012). Structural and metamorphic features of the Main Central Thrust Zone and its contiguous domains in the eastern Nepalese Himalaya. *Journal of Virtual Explorer, Electronic Edition, 41*, paper 2.

Moynihan, D. P., & Pattison, D. R. M. (2013). An automated method for the calculation of P-T paths from garnet zoning, with application to metapelitic schist from the Kootenay Arc, British Columbia, Canada. *Journal of Metamorphic Geology, 31*, 525–548.

Nagurney, A. B., Caddick, M. J., Dragovic, B., & Busse, K. (2021). The (chemical) potential for understanding overstepped garnet nucleation and growth. *American Mineralogist, 106*, 812–829.

Parrish, R. R., & Hodges, K. V. (1996). Isotopic constraints on the age and provenance of the Lesser Himalaya. *Geological Society of America Bulletin, 108*, 904–911.

Pattison, D. R. M., & Tinkham, D. K. (2009). Interplay between equilibrium and kinetics in prograde metamorphism of pelites: an example from the Nelson aureole, British Columbia. *Journal of Metamorphic Geology, 27*, 249–279.

Pattison, D. R. M., de Capitani, C., & Gaidies, F. (2011). Petrological consequences of variations in metamorphic reaction affinity. *Journal of Metamorphic Geology, 29*, 953–977.

Pearson, O. N., & DeCelles, P. G. (2005). Structural geology and regional tectonic significance of the Ramgarh thrust, Himalayan fold-thrust belt of Nepal. *Tectonics, 24*, TC4008.

Pêcher, A. (1989). The metamorphism in Central Himalaya. *Journal of Metamorphic Geology, 7*, 31–41.

Pouchou, J. L. & Pichoir, F. (1988). Determination of mass absorption coefficients for soft X-rays by use of the electron microprobe. In: Newbury, D. E. (eds.) Microbeam Analysis. San Francisco, CA, San Francisco Press, 319-324.

Powell, R., Guiraud, M., & White, R.W. (2005). Truth and beauty in metamorphic phase-equilibria: conjugate variables and phase diagramas. *Canadian Mineralogist, 43*, 21–33.

Powell, R., & Holland, T. J. B. (2008). On thermobarometry. *Journal of Metamorphic Geology, 26*, 155–179.

Rai, S. M., Guillot, S., Le Fort, P., & Upreti, B.N. (1998). Pressure-temperature evolution in the Kathmandu and Gosainkund regions, Central Nepal. *Journal of Asian Earth Sciences, 16*, 283–298.

Rapa, G., Groppo, C., Mosca, P., & Rolfo, F. (2016). Petrological constrains on the tectonic setting of the Kathmandu Nappe in the Langtang-Gosainkund-Helambu regions, Central Nepal Himalaya. *Journal of Metamorphic Geology, 34*, 999–1023.

Rapa, G., Groppo, C., Rolfo, F., Petrelli, M., Mosca, P., & Perugini, D. (2017). Titanite-bearing calc-silicate rocks constrain timing, duration, and magnitude of metamorphic CO_2 degassing in the Himalayan belt. *Lithos, 292–293*, 364–378.

Rapa, G., Mosca, P., Groppo, C., Rolfo, F. (2018). Detection of tectonometamorphic discontinuities within the Himalayan orogen: Structural and petrological constraints from the Rasuwa district, central Nepal Himalaya. *Journal of Asian Earth Sciences*, 158, 266–286.

Robinson, D. M., DeCelles, P. G., Patchett, P. J., & Garzione, C. N. (2001). The kinematic history of the Nepalese Himalaya interpreted from Nd isotopes. *Earth and Planetary Science Letters, 192*, 507–521.

Rolfo, F., Groppo, C. & Mosca, P. (2015). Petrological constraints of the “Channel Flow” model in eastern Nepal. In: Mukherjee, S., Carosi, R., van der Beek, P. A., Mukherjee, B. K., & Robinson, D. M. (eds), “Tectonics of the Himalaya”. *Geological Society of London, Special Publications, 412*, 177–197.

Searle, M. P., Law, R. D., Godin, L., Larson, K. P., Streule, M. J., Cottle, J. M., & Jessup, M. J. (2008). Defining the Himalayan Main Central Thrust in Nepal. *Journal of the Geological Society of London, 165*, 523–534.

Spear, F. S. (1993). Metamorphic phase equilibria and pressure–temperature–time paths. *Mineralogical Society of America Monograph, 1*, 799 pp.

Spear, F. S., Thomas, J. B., & Hallett, B. W. (2014). Overstepping the garnet isograd: a comparison of QuiG barometry and thermodynamic modeling. *Contributions to Mineralogy and Petrology, 168*, 1–15.

Spear, F. S., & Wolfe, O. M. (2018). Evaluation of the effective bulk composition (EBC) during growth of garnet. *Chemical Geology, 491*, 39–47.

Spear, F. S., & Wolfe, O.M. (2019). Implications of overstepping of garnet nucleation for geothermometry, geobarometry and P-T path calculations. *Chemical Geology, 530*, 119323

Stöcklin, J. (1980). Geology of Nepal and its regional frame. *Journal of the Geological Society of London, 137,* 1–34.

Terry, M. P., & Heidelbach, F. (2006). Deformation-enhanced metamorphic reactions and the rheology of high-pressure shear zones, Western Gneiss Region, Norway. *Journal of Metamorphic Geology, 24*, 3–18.

Tinkham, D.K., & Ghent, E. D. (2005) Estimating P-T conditions of garnet growth with isochemical phase-diagram sections and the problem of effective bulk-composition. *Canadian Mineralogist*, *43*, 35–50.

Ulmer, P. (1986). NORM. Program for cation and oxygen mineral norms. Computer Library, Institut für Mineralogie und Petrographie, ETH-Zentrum, Zürich, Switzerland.

Upreti, B. N. (1999). An overview of the stratigraphy and tectonics of the Nepal Himalaya. *Journal of Asian Earth Science, 17*, 577–606.

Valdiya, K.S. (1980). Geology of the Kumaun Lesser Himalaya. Wadia Institute of Himalayan Geology, Dehradun, India, 289 pp.

Wang, J.-M., Zhang, J.-J., Liu, K., Wang, X.-X., Rai, S., & Scheltens, M. (2016). Spatial and temporal evolution of tectonometamorphic discontinuities in the Central Himalaya: Constraints from P-T paths and geochronology. *Tectonophysics, 679*, 41–60.

Waters, D. J. (2019). Metamorphic constraints on the tectonic evolution of the High Himalaya in Nepal: the art of the possible. In: Himalayan Tectonics: A Modern Synthesis (Treloar, P. J. & Searle M. P., eds), *Geological Society, London, Special Publications, 483*, 325–375.

Waters, D. J., & Lovegrove, D. P. (2002). Assessing the extent of disequilibrium and overstepping of prograde metamorphic reactions in metapelites from the Bushveld complex aureole, South Africa. *Journal of Metamorphic Geology, 20*, 135–149.

White, R. W., Powell, R., & Johnson, T. E. (2014). The effect of Mn on mineral stability in metapelites revisited: New a–x relations for manganese-bearing minerals. *Journal of Metamorphic Geology, 32*, 809–828.

White, R. W., Powell, R., & Holland, T. J. B. (2007). Progress relating to calculation of partial melting equilibria for metapelites. *Journal of Metamorphic Geology, 25*, 511–527.

Whitney, D. L., & Evans, B. W. (2010). Abbreviations for names of rock-forming minerals. *American Mineralogist, 95,* 185–187.

Wolfe, O. M., & Spear, F. S. (2018). Determining the amount of overstepping required to nucleate garnet during Barrovian regional metamorphism, Connecticut Valley Synclinorium. *Journal of Metamorphic Geology, 36*, 79–94.

Yin, A., & Harrison, T.M. (2000). Geologic evolution of the Himalayan-Tibetan orogen. *Earth and Planetary Sciences Letters, 28*, 211–280.

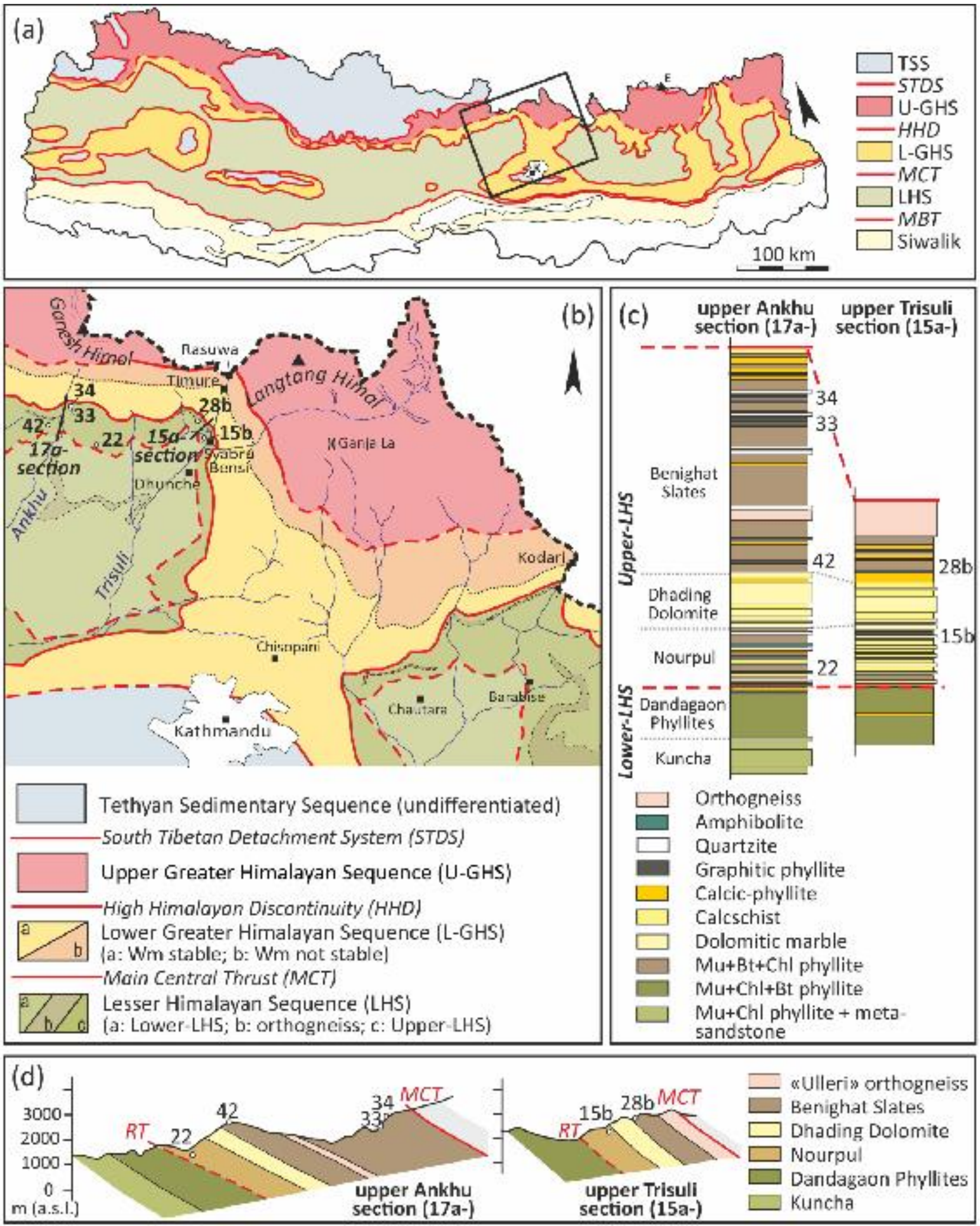

Fig. 1 – (a) Geological sketch map of the Nepal Himalaya, showing the major tectono-metamorphic units (modified from Dhital, 2015 and He et al., 2015). The location of the High Himalayan Discontinuity (HHD) is based on Groppo et al. (2009, 2010, 2012, 2013), Mosca et al. (2012), Rolfo et al. (2015) and Rapa et al. (2016, 2017, 2018) for central-eastern Nepal and on Montomoli et al. (2013) and Wang et al. (2016) for central-western Nepal. The black rectangle indicates the location of (b). LHS: Lesser Himalayan Sequence, L-GHS: Lower Greater Himalayan Sequence, U-GHS: Upper Greater Himalayan Sequence, TSS: Tethyan Sedimentary Sequence; MBT: Main Boundary Thrust, MCT: Main Central Thrust, HHD: High Himalayan Discontinuity, STDS: South Tibetan Detachment System; K: Kathmandu, E: Everest. (b) Geological sketch map of the region north of Kathmandu with location of the

studied samples (modified from Rapa et al., 2016, 2018). (c) Schematic stratigraphic columns of the two studied sections (upper Ankhu section: samples 17a-; upper Trisuli section: samples 15a-) reported in (b), with indication of the main lithologies and location of the studied samples. The different Formations are distinguished according to the classification of Stöcklin (1980) and Upreti (1999). (d) Simplified geological profiles along the upper Ankhu and upper Trisuli transects reported in (b), with location of the studied samples.

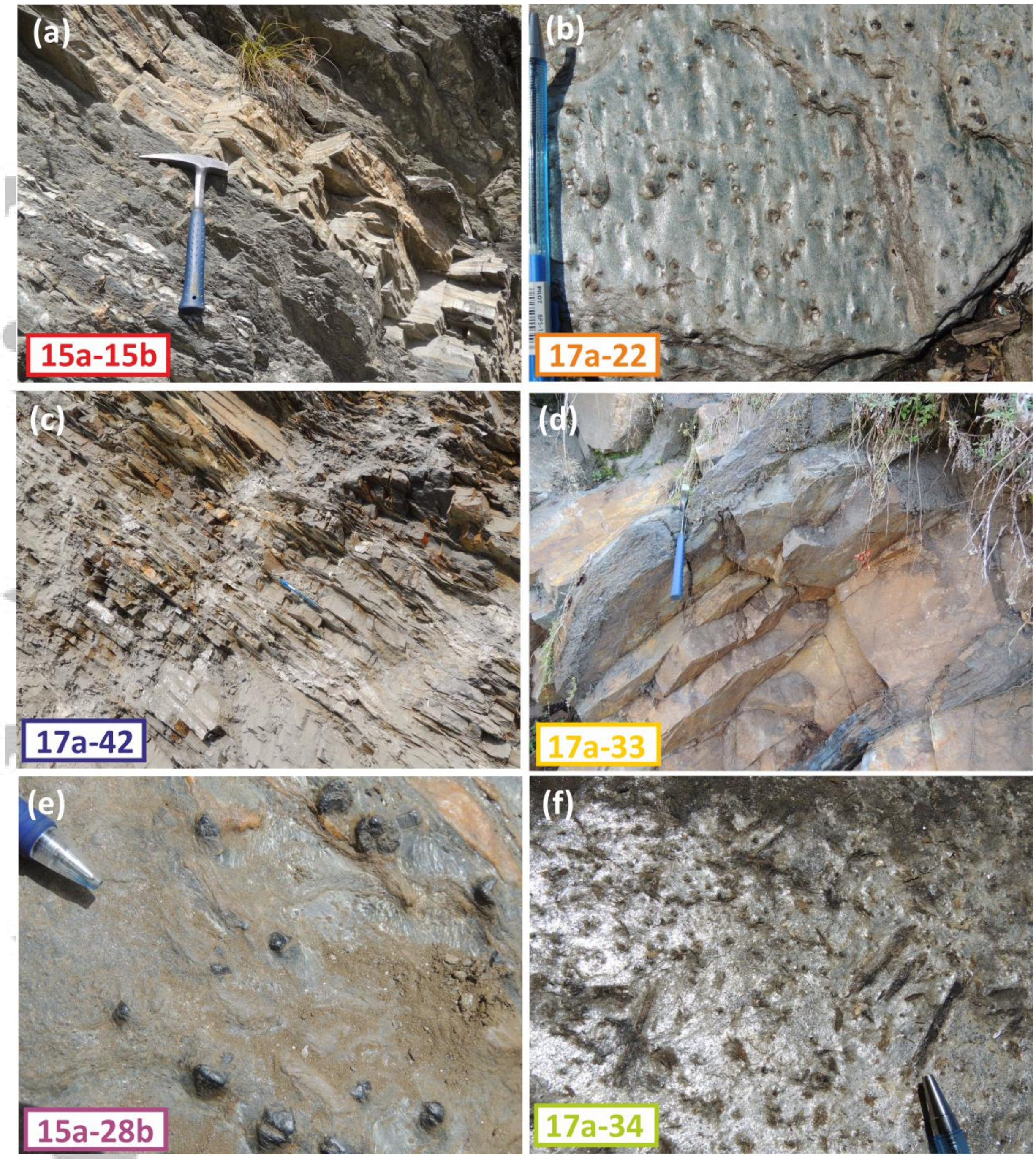

Fig. 2 – Outcrop images representative of the Nourpul Formation (a,b) and Benighat Slates (c-f) from which the studied samples have been collected. (a) Metric layers of graphitic phyllites intercalated with banded quartzites (sample 15a-15b). (b) Chlorite + muscovite phyllite with garnet porphyroblasts (sample 17a-22). (c) Graphitic phyllites alternated with calcic-phyllites in decametric-thick layers (sample 17a-42). (d) Thin layers of graphitic phyllites intercalated with metric layers of quartzites (sample 17a-33). (e) Multi-millimetric garnet and staurolite (top right) porphyroblasts in a graphitic phyllite from the Benighat Slates (sample 15a-28b). (f) Staurolite and kyanite porphyroblasts up to few centimetres in length in a graphitic phyllite (sample 17a-34).

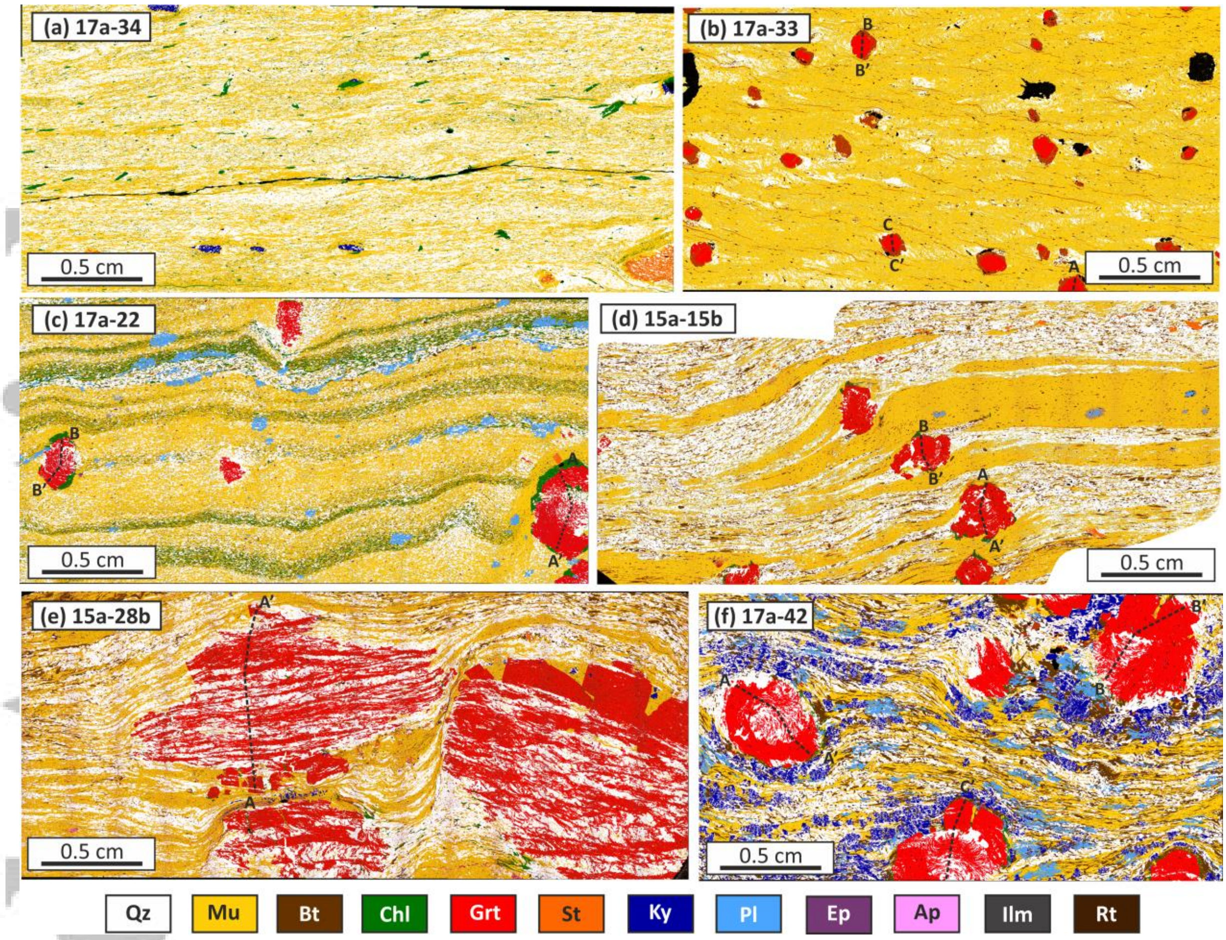

Fig. 3 – Processed X-Ray maps of the studied samples: (a) 17a-34; (b) 17a-33; (c) 17a-22; (d) 15a-15b; (e) 15a-28b; and (f) 17a-42. Compositional profiles of garnet porphyroblasts carried out along the transects reported in (b) to (f) are reported in Supplementary Fig. SM1.

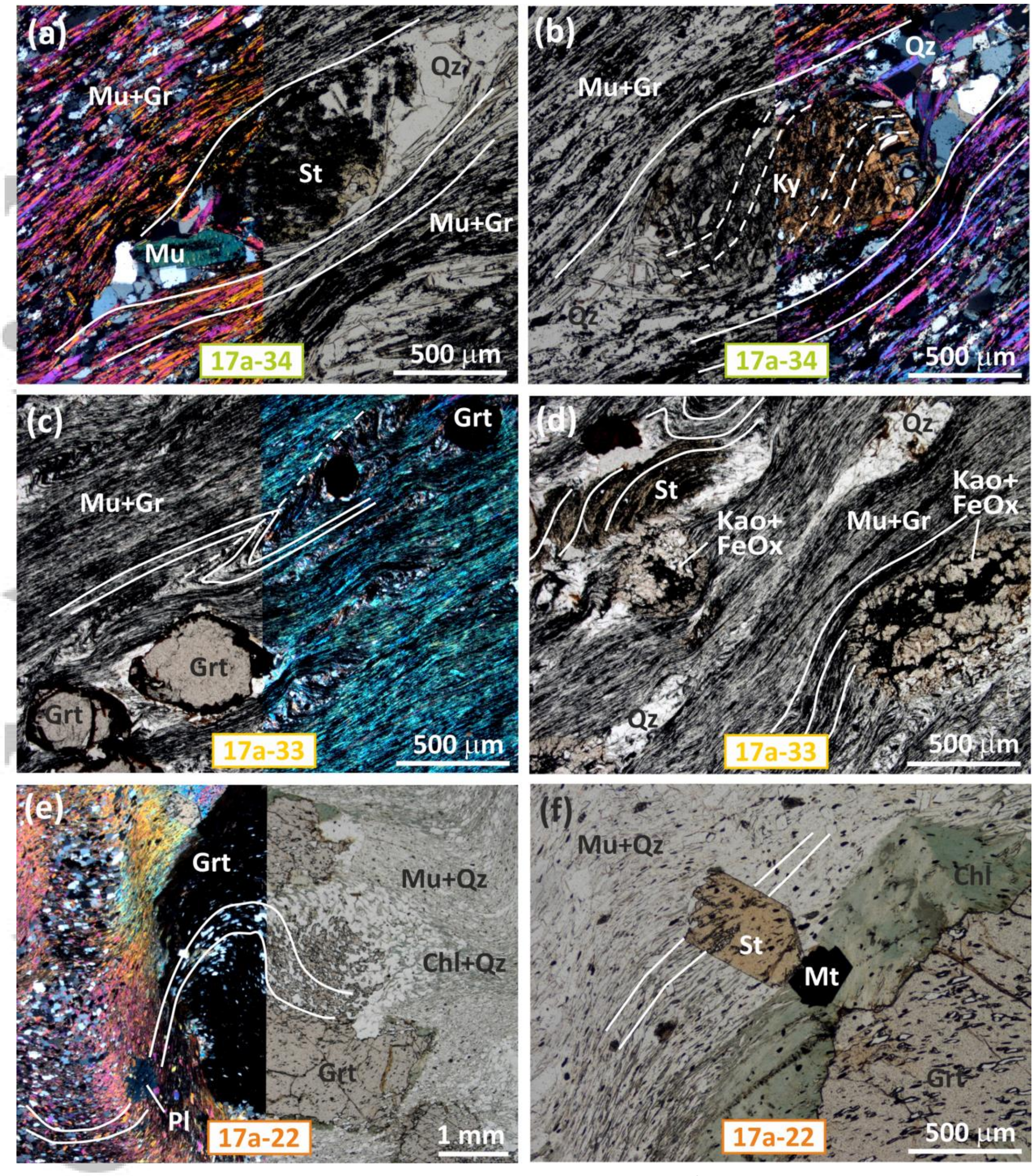

Fig. 4 – Representative assemblages and microstructures of samples 17a-34, 17a-33 and 17a-22. White lines in all the pictures are: S_m = continuous; S_{m-1} = dashed; S_{m+1} = dotted-dashed. Sample 17a-34: (a) Staurolite porphyroblasts enveloped by the S_m defined by muscovite (left: Crossed Polarized Light, XPL; right: Plane Polarized Light, PPL). (b) Kyanite porphyroblast wrapped around by the S_m and including an internal rotated foliation defined by quartz and muscovite (left: PPL; right: XPL). Sample 17a-33: (c) Garnet porphyroblasts in equilibrium with the S_m, but pre-kinematic with respect to the S_{m+1}. Note the dark brown, oxidized rim of garnet (left: PPL; right: XPL). (d) Staurolite occuring as rare porphyroblasts overgrowing the S_m and enveloped by the S_{m+1}. Large aggregates of kaolinite + Fe-oxides overgrow the S_m and likely replace a former plagioclase (PPL). Sample 17a-22: (e) Multi-mm

garnet porphyroblast including a rotated internal foliation mostly continuous with the external S_m (left: XPL; right: PPL). (f) The post-kinematic garnet rim is completely replaced by late chlorite. Staurolite porphyroblast overgrows the S_m defined by muscovite and chlorite (PPL).

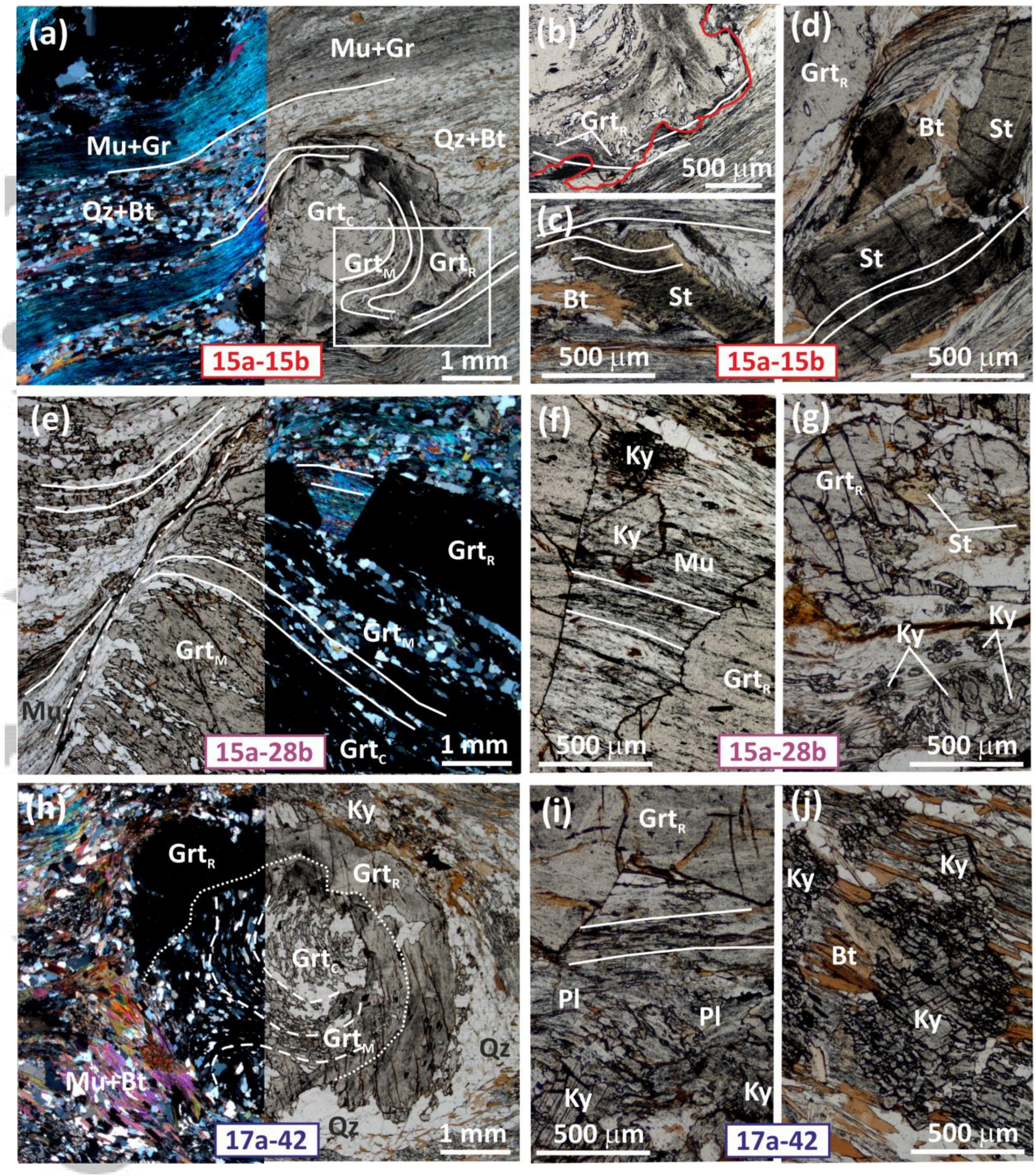

Fig. 5 – Representative assemblages and microstructures of samples 15a-15b, 15a-28b and 17a-42. White lines are defined as in Fig. 4. Sample 15a-15b: (a) Garnet porphyroblasts including a rotated internal foliation continuous with the external S_m. GrtC and GrtM are syn-kinematic with respect to S_m, whereas GrtR statically overgrows it. The inset refers to detail reported in (b) (left: XPL; right: PPL). (b) Detail of (a) highlighting the post-kinematic relations of garnet rim with respect to the S_m (PPL). The red line marks the garnet border. (c) Syn-kinematic staurolite porphyroblasts including an internal foliation defined by graphite, continuous with the external S_m (PPL). (d) Post-kinematic staurolite porphyroblasts statically overgrowing the S_m (PPL). Sample 15a-28b: (e) Centimetric garnet porphyroblast with a skeletal core and a post-kinematic rim overgrowing the S_m (left: PPL; right: XPL). (f) Detail of

the garnet rim overgrowing the S_m; kyanite porphyroblasts are also post-kinematic with respect to the S_m (PPL). (g) Post-kinematic staurolite and kyanite developed close to garnet rim (PPL). Sample 17a-42: (h) Garnet porphyroblast characterised by two distinct domains: a pre-kinematic Grt_C + Grt_M, including a rotated internal foliation (S_{m-1}) discontinuous with respect to the external S_m, and a post-kinematic Grt_R, statically overgrowing the S_m (left: XPL; right: PPL). (i) Detail of garnet rim, plagioclase and kyanite statically overgrowing the S_m (PPL). (j) Kyanite porphyroblasts overgrow the main foliation defined by biotite and muscovite (PPL).

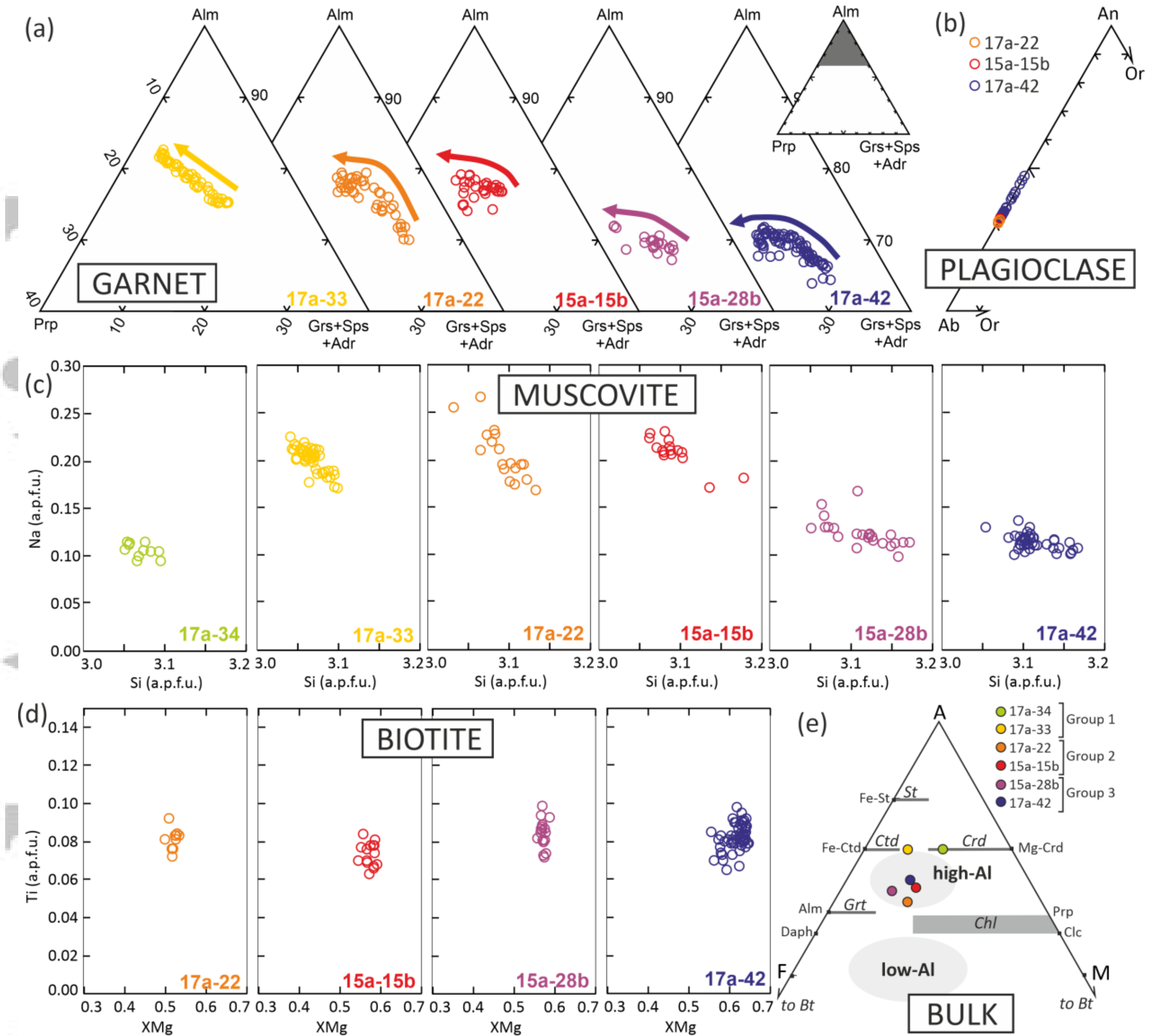

Fig. 6 – Compositional diagrams for garnet (a; arrows show the zoning trend from garnet core to garnet rim), plagioclase (b), muscovite (c) and biotite (d), and bulk compositions of the studied samples (e) plotted in the AFM diagram projected from muscovite (quartz and H_2O in excess). The low-Al and high-Al metapelite fields in (e) are from Spear (1993).

Fig. 7 – Blastesis-deformation diagrams for the studied metapelites. Black lines represent clearly stable phases; grey lines represent phases presumed to be stable on the basis of microstructural observations and/or completely replaced by late phases. S_m is the main foliation; S_{m-1} and S_{m+1} developed earlier and later than S_m, respectively. Δ refers to the static growth of the peak mineral assemblage.

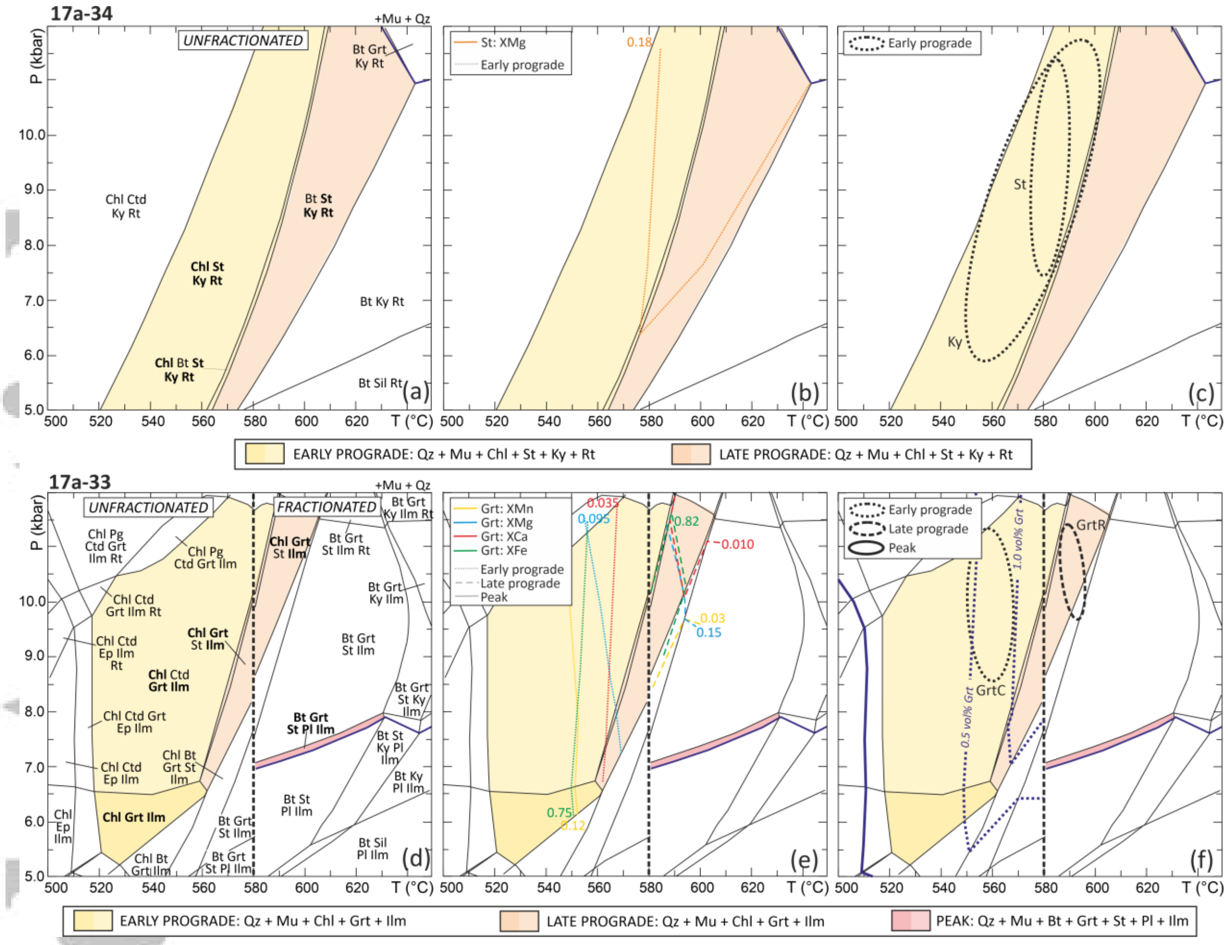

Fig. 8 – P–T isochemical phase diagrams modelled for sample 17a-34 (a-c) and 17a-33 (d-f) using the measured bulk-compositions (unfractionated: on the left in d-f), and the effective bulk compositions after fractionation of garnet core + mantle (fractionated: on the right in d-f). The variance of the fields varies from two (i.e. 7 phases) to four (i.e. 5 phases) for sample 17a-34 (a), and from three (i.e. 9 phases) to seven (i.e. 5 phases) for sample 17a-33 (d). Early prograde, late prograde and peak assemblages corresponding to those reported in Fig. 7 are indicated in yellow, orange and red, respectively, with darker tones highlighting the best fit between the observed and the modelled assemblages (for each modelled assemblage, the observed minerals are reported in bold). The modelled compositional isopleths are reported in (b) and (e); the correspondent uncertainties are reported in Supplementary Fig. SM3. Dotted and dashed isopleths refer to composition of early prograde and late prograde phases. The black ellipses in (c) and (f) summarize the P-T conditions constrained for the growth of each mineral, based on the intersection or overlap of the correspondent compositional isopleths (see also Supplementary Fig. SM3) reported in (b) and (e). The different line styles of the ellipses refer to early prograde and late prograde phases, as indicated in the legends. The thick continuous blue lines in (c) and (f) are the Grt-in boundary curves; dotted blue lines in (f) refer to 0.5% and 1.0% garnet isomodes.

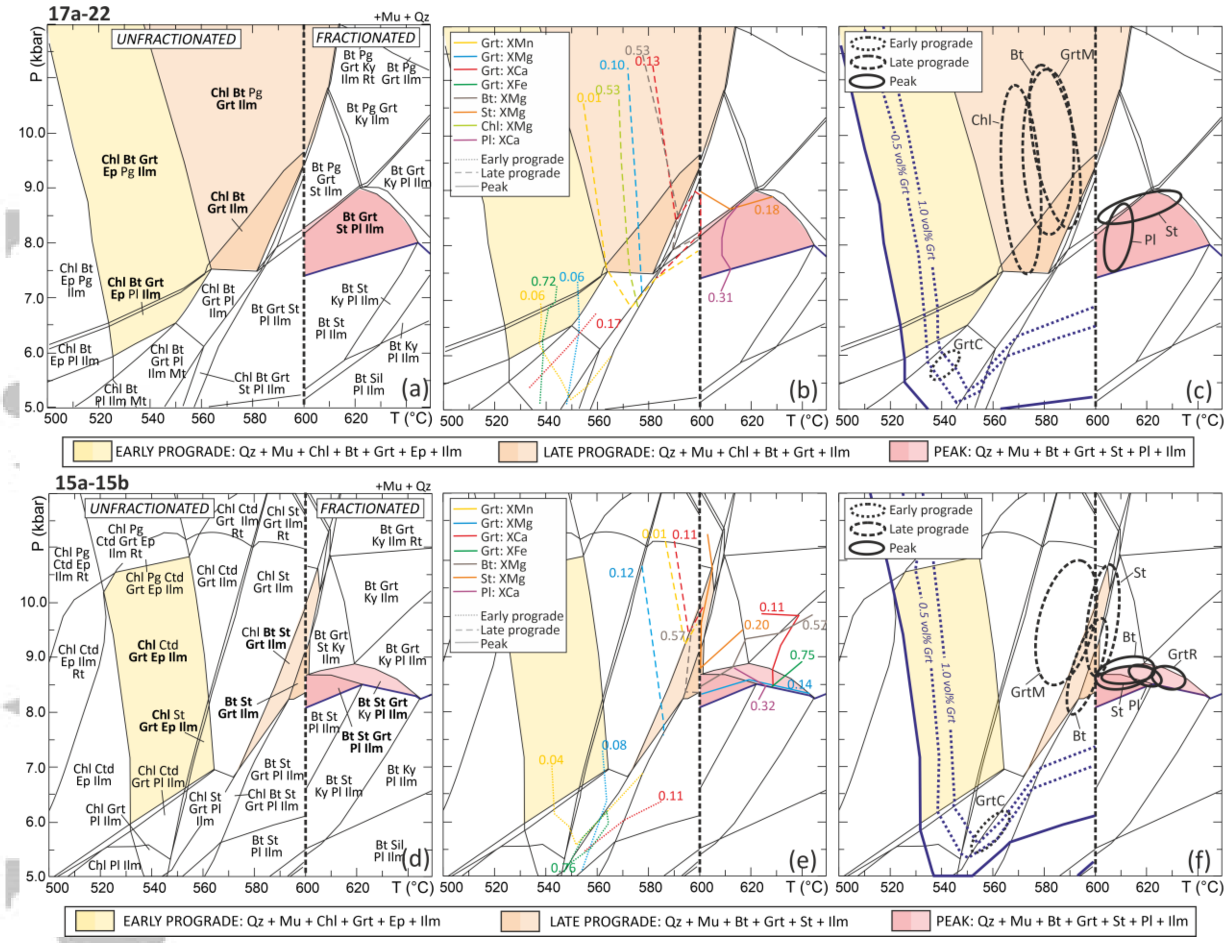

Fig. 9 – P–T isochemical phase diagrams modelled for sample 17a-22 (a-c) and 15a-15b (d-f) using the measured bulk-compositions (unfractionated: on the left in all the diagrams), and the effective bulk compositions after fractionation of garnet core + mantle (fractionated: on the right in all the diagrams). The variance of the fields varies from three (i.e. 9 phases) to six (i.e. 6 phases) for sample 17a-22 (a), and from three (i.e. 9 phases) to seven (i.e. 5 phases) for sample 15a-15b (d). Colours and lines as in Fig. 8 with the addition of continuous isopleth lines in (b) and (e) referring to compositions of peak phases and of continuous ellipses in (c) and (f), referring to the P-T conditions constrained for the growth of peak assemblage. Uncertainties for compositional isopleths of each phase are reported in Supplementary Figs. SM4 and SM5.

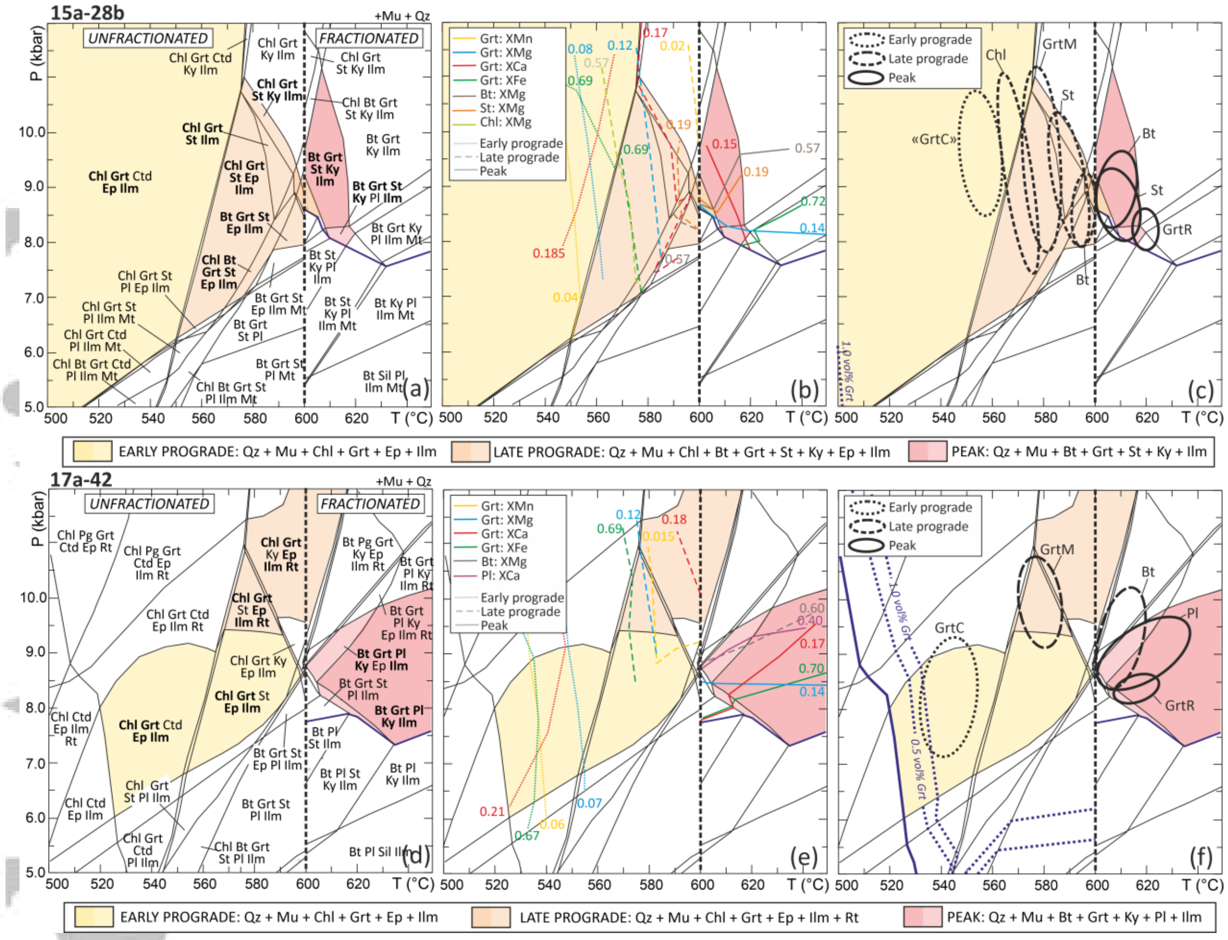

Fig. 10 – P–T isochemical phase diagrams modelled for sample 15a-28b (a-c) and 17a-42 (d-f) using the measured bulk-compositions (unfractionated: on the left in all the diagrams), and the effective bulk compositions after fractionation of garnet core + mantle (fractionated: on the right in all the diagrams). The variance of the fields varies from three (i.e. 9 phases) to six (i.e. 6 phases) for both samples 15a-28b (a) and 15a-15b (d). Colours and lines as in Figs. 8–9. Uncertainties for compositional isopleths of each phase are reported in Supplementary Figs. SM6 and SM7.

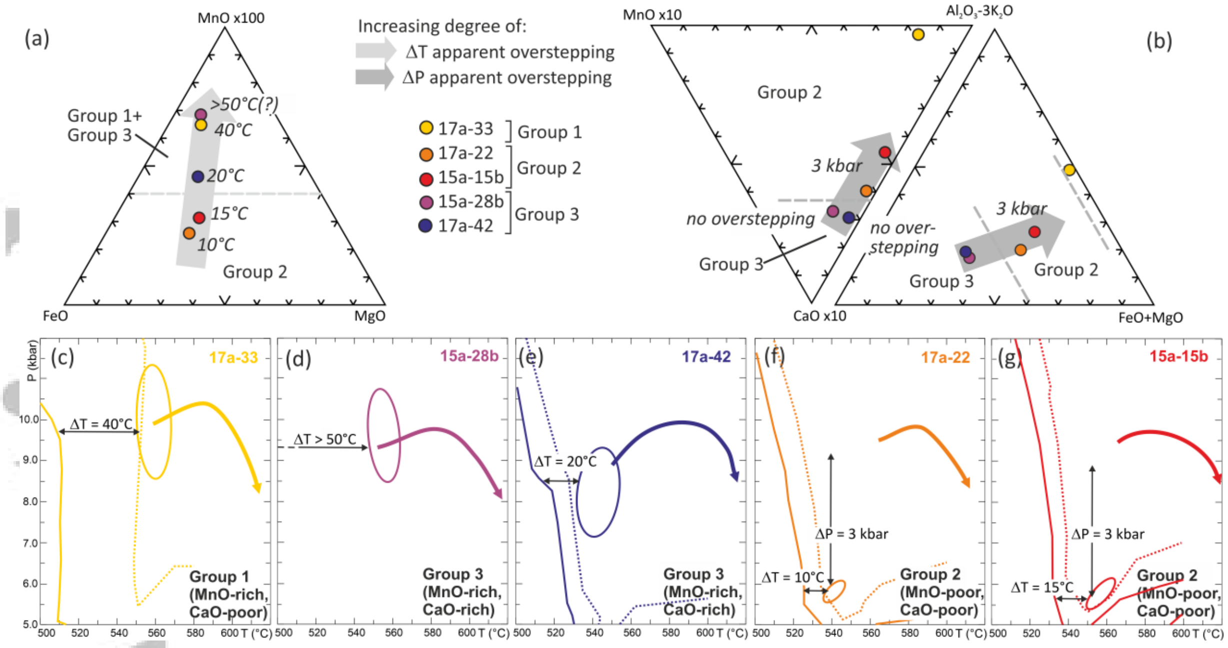

Fig. 11 – (a-c) Bulk compositions of the studied samples plotted in ternary diagrams. This representation emphasizes the main differences between the three compositional groups. The bulk MnO content appears strongly correlated with the apparent ΔT overstepping of garnet nucleation (light grey arrow in a). The bulk CaO content seems correlated with the apparent ΔP overstepping of garnet nucleation (dark grey arrows in b and c). (c-g) Summary of the early prograde P-T conditions inferred for the growth of garnet core (ellipses) and apparent ΔT and ΔP overstepping of garnet nucleation. Continuous and dotted lines are the garnet-in curves and the 0.5% garnet isomodes. The coloured arrows represent the P-T paths reconstructed for each sample (see Fig. 12).

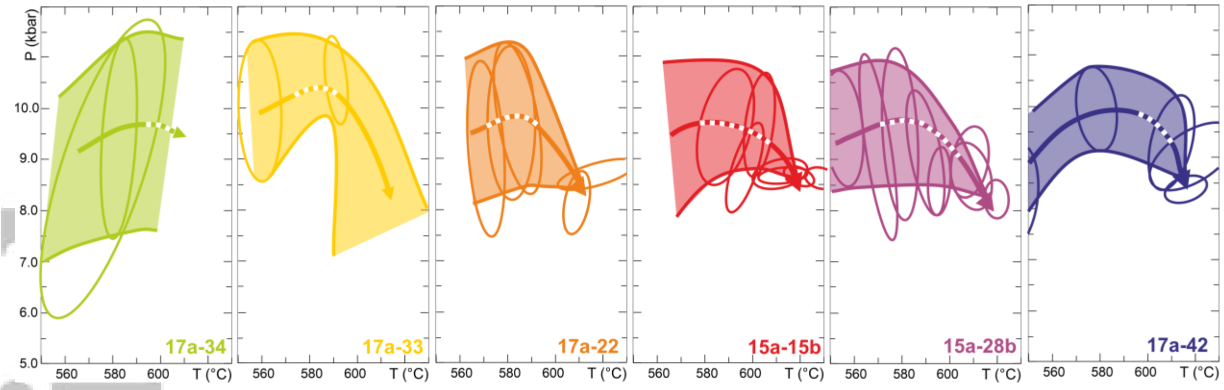

Fig. 12 – P-T grids summarizing the P-T paths reconstructed for the studied metapelites. The ellipses are the same reported in Figs. 8–10 (panels (c) and (f)). The large, coloured paths envelope the ellipses; the thin arrows are traced in the middle of each envelope. The dashed white portion of the arrows constrain the development of the main foliation S_m in each sample. Note that, in spite of the relatively large uncertainties on the estimated prograde pressures, all the reconstructed P-T paths show a common shape.

Table 1. Modal compositions (vol%) and location of the modelled metapelites

Sample	Qz	Mu	Bt	Chl	GrtC+M	GrtR	St	Ky	Pl	Ilm	Rt	GPS coordinates
17a-34	54.8	36.8	-	4.5	-	-	2.3	1.6	-	-	<0.1	N28°13'55.5''; E85°05'02.8'' - 2655 m
17a-33	13.0	80.4	4.0	0.0	1.0	0.7	0.0	0.0	0.0	0.9	0.0	N28°13'42.1''; E85°05'09.0'' - 2475 m
17a-22	30.2	47.0	2.3	9.3	1.4	3.4	1.1	-	4.8	0.5	-	N28°10'00.8''; E85°08'01.0'' - 2760 m
15a-15b	38.2	42.1	8.9	1.3	2.0	3.2	2.5	-	1.3	0.5	-	N28°10'10.1''; E85°20'00.0'' - 1980 m
15a-28b	40.1	23.9	6.2	2.7	18.3	3.2	2.1	3.4	-	<0.1	-	N28°11'51.1''; E85°18'30.6'' - 2615 m
17a-42	35.0	20.3	13.9	0.0	4.7	11.0	0.0	8.2	6.5	0.1	0.3	N28°11'51.9''; E85°02'34.7'' - 2660 m

Table 2. Effective bulk compositions (mol%) of the modelled metapelites

	17a-34	17a-33		17a-22		15a-15b		15a-28b		17a-42	
	MBC	MBC	MBC-(GrtC + GrtM)	MBC	MBC-(GrtC + GrtM)	MBC	MBC-(GrtC + GrtM)	MBC	MBC-(GrtC + GrtM)	MBC	MBC-(GrtC + GrtM)
SiO_2	81.54	64.32	64.67	68.21	68.73	72.27	73.14	68.23	76.20	67.33	68.97
TiO_2	0.19	1.25	1.27	0.49	0.50	0.62	0.64	0.15	0.19	0.68	0.73
Al_2O_3	11.52	22.15	22.28	14.52	14.53	13.91	13.90	12.83	12.38	14.23	14.23
Fe_2O_3	0.00	0.17	0.15	0.19	0.17	0.13	0.11	0.26	0.11	0.21	0.17
FeO	1.80	3.30	2.85	7.29	6.83	5.28	4.49	10.26	4.43	8.21	6.84
MnO	0.00	0.09	0.01	0.04	0.00	0.04	0.00	0.31	0.00	0.11	0.00
MgO	2.03	1.42	1.36	4.04	4.07	3.37	3.35	3.76	3.59	4.43	4.50
CaO	0.00	0.02	0.00	0.76	0.63	0.43	0.30	2.10	0.33	2.03	1.62
Na_2O	0.36	1.53	1.55	1.19	1.22	0.88	0.91	0.24	0.32	0.65	0.69
K_2O	2.56	5.76	5.85	3.26	3.33	3.07	3.16	1.86	2.45	2.11	2.25
Total	100.00	100.00	100.00	100.00	100.00	100.00	100.00	100.00	100.00	100.00	100.00